Spring 2021

Carbonatite Metasomatism and Water Systematics of Peridotite Xenoliths From Lanzarote, Canaries

Sierra N. Patterson

Recommended Citation

Patterson, S. N.(2021). *Carbonatite Metasomatism and Water Systematics of Peridotite Xenoliths From Lanzarote, Canaries.* (Master's thesis). Retrieved from https://scholarcommons.sc.edu/etd/6204

CARBONATITE METASOMATISM AND WATER SYSTEMATICS OF PERIDOTITE XENOLITHS FROM LANZAROTE, CANARIES

by

Sierra N. Patterson

Bachelor of Science
University of Delaware, 2019

Submitted in Partial Fulfillment of the Requirements

For the Degree of Master of Science in

Geological Sciences

College of Arts and Sciences

University of South Carolina

2021

Accepted by:

Michael Bizimis, Director of Thesis

Besim Dragovic, Reader

Gene Yogodzinski, Reader

Tracey L. Weldon, Interim Vice Provost and Dean of the Graduate School

ABSTRACT

Water in Earth's mantle, present as structurally bound hydrogen in minerals, influences large scale processes like mantle deformation, plate tectonics, and melting. To better understand the processes controlling water concentrations in the Earth's upper mantle, we analyzed hydrogen (calculated as ppm wt. H_2O), major, and trace element concentrations in minerals from peridotite mantle xenoliths of Lanzarote, Canaries. The Canaries Islands are thought to be the surface expression of a deep-seated mantle plume erupting through the Atlantic Ocean lithosphere. Carbonatite magmas have erupted in the Canaries and previous studies have shown evidence for carbonatite metasomatism in Lanzarote peridotites. Thus, the Canaries offer a rare opportunity to examine the role of carbonatite metasomatism as a mechanism in rehydrating the oceanic lithosphere during plume-lithosphere interaction.

Peridotites in this study are found as xenoliths in Quaternary to recent basaltic lavas of the Timanfaya volcanic series on the island of Lanzarote. Major element data show that these peridotites are highly depleted compared to the primitive mantle, with a high average olivine Mg# (91.1 ± 0.5), low bulk rock Al_2O_3 (0.4 to 1.4 wt.%), high spinel Cr# (40 to 72) from which high degrees of melting were estimated (15 to 21%). Trace element data in orthopyroxene, clinopyroxene, and bulk rock frequently show high La/Yb ratios (up to 12.2, 71.5, 45.2; respectively) and strong negative Zr, Hf, and Ti anomalies relative to REE, consistent with carbonatite metasomatism. There is no evidence of hydrous phases (e.g., amphibole and phlogopite), thus water in these peridotites is thought to be stored only in nominally anhydrous minerals and melt inclusions. Water concentrations (determined by polarized FTIR spectroscopy), in the peridotite silicate minerals range from 2.7 to 13 ppm in olivine, 42 to 265 ppm in orthopyroxene (Opx), and 76 to 470 ppm in clinopyroxene (Cpx). Reconstructed bulk rock water concentrations range from 5 to 115 ppm, generally lower than estimates for the depleted mantle (DM, 50-200 ppm), but significantly higher than expected from the degree of depletion. With decreasing Ti/Eu_{cpx} ratios, a proxy for carbonatite metasomatism, the bulk water and clinopyroxene water increases. The calculated trace element compositions of melts in equilibrium with Cpx strongly resemble those of carbonatites. However, the bulk rock water concentrations are two orders of magnitude lower than what is expected by equilibrium with a carbonatite melt. We conclude that while carbonatitic metasomatism did rehydrate the Lanzarote mantle lithosphere it did so to a much lesser extent than expected, implying lower partitioning of H in the presence of CO_2 than a silicate melt. Therefore, the inference for volatile-rich metasomatism from carbonatitic melts does not translate to excess water addition in the oceanic lithosphere.

TABLE OF CONTENTS

LIST OF TABLES

LIST OF FIGURES

LIST OF SYMBOLS

1σ	Standard deviation.
α	Optical axis alpha of a crystallographic optical indicatrix.
$A(n)$	Integrated absorbance for respective optical orientations
β	Optical axis beta of a crystallographic optical indicatrix.
Bxa	Bicectrix acute.
Bxo	Bicectrix obtuse.
$D_i^{A/B}$	Partitioning coefficient (D) of element i into material A over material B.
$E\|\alpha$	parallel to predetermined refractive indicatrix α.
$E\|\beta$	parallel to predetermined refractive indicatrix β.
$E\|\gamma$	parallel to predetermined refractive indicatrix γ.
I'	Inverse of molar absorbance coefficient (μ).
$\log D$	Log of diffusion coefficient.
μ	Molar absorbance coefficient.
γ	Optical axis gamma of a crystallographic optical indicatrix.

LIST OF ABBREVIATIONS

ARES	Astromaterials Research and Explorative Science
CEM	Center of Elemental Mass Spectroscopy
BR	Bulk Rock
BSE	Back Scatter Electron
DM	Depleted Mantle
DMM	Depleted MORB Mantle
EM	Enriched Mantle
EMP	Electron Micro-probe
FTIR	Fourier Transform Infrared Spectroscopy
HREE	Heavy Rare Earth Element
LA-ICPMS	Laser Ablation-Inductively Coupled Plasma-Mass Spectrometry
LBLZ23-	sample prefix denoting Montana Colorada volcanic province
LBLZ25-	sample prefix denoting Salinas de Janubio province

LBLZ27-	sample prefix denoting Caldera de los Cuervos volcanic province
LBLZ36-	sample prefix denoting El Cuchillo volcanic province
LREE	Light Rare Earth Element
MCT	Mercury Cadmium Telluride
MORB	Mid-Ocean Ridge Basalt
NAM	Nominally Anhydrous Mineral
NASA	National Aeronautics and Space Administration
OIB	Ocean Island Basalt
ON	Optical Normal
PM	Primitive Mantle
ppm	parts per million weight percent (concentration)
REE	Rare Earth Element
SEM	Scanning Electron Microscope
SLC	Salt Lake Crater
UofSC	University of South Carolina
USGS	United States Geological Survey

wt.%	weight percent (concentration)
XRF	X-Ray Florescence

CHAPTER 1

INTRODUCTION

Understanding the water systematics of the Earth’s mantle is imperative because hydrogen strongly influences mantle deformation, melting, and metasomatism as well as seismic anisotropy, electrical conductivity, rheology, volcanism, magmatism, and tectonic processes (e.g., Justice et al., 1982; Chopra and Paterson, 1984; Karato, 1990; Hirose and Kawamoto, 1995; Hirth and Kohlstedt, 1996; Médard and Grove, 2008; Peslier et al., 2010). For example, the presence of hydrogen weakens the olivine structure making it more susceptible to deformation (e.g., Demouchy et al., 2012; Tielke et al., 2017). Water discussed here and thereafter refers to hydrogen trapped in crystal defects of silicate mineral structures, calculated as parts per million by weight H_2O (ppm wt. H_2O). Nominally anhydrous minerals (NAMs; e.g., olivine [Ol], orthopyroxene [Opx], clinopyroxene [Cpx], garnet) in the Earth’s mantle and lithosphere contain <0.1 weight % water (Peslier et al., 2017). Even though this is a small percentage when compared to hydrous phases thought to exist deeper in the convecting mantle, like hydrous wadsleyite and hydrous ringwoodite (up to 3.3 wt. % H_2O; Kawamoto, 2006 and sources therein), NAMs are the main water reservoirs for the upper mantle (shallower than 400 km). Despite the importance of water concentrations in the upper mantle, its distribution and mechanisms that control water concentrations remain poorly understood.

It is estimated that greater than one mass the Earth’s oceans are stored as H in NAMs in the mantle (Peslier et al., 2017). Estimated water concentrations for the Earth’s main mantle reservoirs are 330 to 1100 ppm for primitive mantle (PM), 50 to 200 ppm for depleted mantle source of mid-ocean ridge basalt (DM or DMM; MORB; 54 ppm, Simons et al., 2002; 116 ppm, Salters and Stracke, 2004; 150 to 200 ppm, Dixon and Clague, 2001; 70 to 135 ppm, Workman and Hart, 2005; 100 ppm, Hirschmann, 2010; 50 to 200 ppm, Dixon et al., 2002, 1988, Asimow et al., 2004, Green et al., 2010), less than 100 to greater than 400 ppm of enriched mantle (EM) or source of ocean island basalt (OIB) (Bizimis and Peslier, 2015). These estimates come from the composition of erupted lavas, which by their nature may sample more than one lithology and often record magma mixing. Therefore, direct examination of lithospheric peridotites formerly residing closer to the Earth’s convecting mantle can provide additional and unique constraints into the processes that are responsible for variance of water in convecting mantle reservoirs. Previous works suggest peridotite water contents are influenced by a combination of processes such as melt depletion, and subsequent melt and/or fluid percolation. These processes in combination with composition of the mantle source, indicate that peridotites from the oceanic lithosphere have highly variable water contents (e.g., Warren and Hauri, 2014; Peslier et al., 2015; Schaffer et al., 2019; Ashley et al., 2020).

Hydrogen (water) is highly incompatible in the Earth's upper mantle minerals, therefore melting and melt extraction will result in mantle rocks depleted in water. Yet, bulk rock (BR) water contents of oceanic abyssal peridotites from Gakkel Ridge, Tonga Trench, and Southwest Indian Ridge (20 to 220 ppm H_2O) are within and above the DM source estimates, even though these peridotites have experienced melt depletion at the ridge. It is hypothesized that these concentrations are higher due to late-stage melt infiltration and / or hydrothermal alteration (Warren and Hauri, 2014). The large range in water contents of ocean island peridotite xenoliths from Salt Lake Crater, Oahu, Hawaii (SLC; 50 to 96 ppm for peridotite xenoliths and 211 to 467 ppm for pyroxenites, Bizimis and Peslier, 2015; Peslier et al., 2015) and Savai'i, Samoa (1.4 to 23 ppm, Ashley et al., 2020), are consistent with variable levels of melt depletion and metasomatism.

In detail, the SLC peridotites are relatively fertile and their water concentrations have been explained as rehydration of the oceanic lithosphere due to interaction of melts from the rejuvenated stage of the Hawaiian plume and the Pacific lithosphere (Bizimis and Peslier, 2015; Peslier et al., 2015). Savai'i peridotites have water contents much lower than the DM source and have ultra-refractory compositions but are still thought to reflect water addition through a complex silicate + carbonatite melt -lithosphere interaction (Ashley et al., 2020). These studies show each locality has its own complicated water systematics and highly variable water concentrations. Therefore, further investigations of location-specific oceanic peridotite water systematics are needed to interpret how the water contents vary as a function of the two fundamental processes of mantle differentiation: melting and metasomatism.

Peridotite xenoliths from Lanzarote, Canary Islands have experienced high degrees of melt depletion but also are affected by a complex interaction with silicate and carbonatitic melts (Siena et al., 1991; Neumann et al., 1995, 2004; Bhanot et al., 2017). However, Lanzarote peridotite water contents have not been directly measured. Therefore, peridotite xenoliths from Lanzarote offer the opportunity to examine how metasomatism affects the water systematics, focused on emerging hypothesis that carbonatitic metasomatism is not an efficient agent of water addition in the oceanic lithosphere despite its large amounts of water, likely due to the lowered water activity in the melt (Ashley et al., 2020). Here we present the only to-date measured water concentrations of Lanzarote peridotites as well as a complete compositional geochemical dataset. This study aims to reveal the competing effects of melt depletion and metasomatism on water concentrations and to define whether and how mantle plume and lithosphere interaction results in rehydration of the depleted oceanic lithosphere by constraining the effect of metasomatism (carbonatitic and/or silicate) to the rehydration of the mantle lithosphere beneath Lanzarote.

CHAPTER 2

GEOLOGIC BACKGROUND

2.1 Lithospheric mantle of Lanzarote, Canaries

The Canary Islands off the continental margin of northwestern Africa consist of seven islands (Lanzarote, Fuerteventura, Gran Canaria, Tenerife, La Goma, La Palma, El Hierro) with a general East-West age progression (Wilson 1963; Schmincke 1982; Carracedo et al., 1998, Urgeles et al., 1998). The Canaries are thought to represent the surface expression of an active deep-seated asthenospheric mantle plume (Carracedo et al., 1998; Carracedo et al., 2001; Montelli et al., 2005). It is generally accepted that the Canaries reside on the ~125my old Atlantic oceanic lithosphere (Schmincke, 1982, Roest et al., 1992; Neumann et al., 1995). The oceanic lithosphere thickness beneath the Canaries is approximately 90 km thick (Humphreys and Niu, 2009) and presumably of Jurassic age (Neumann et al., 1995) with the MOHO at estimated 11 to 12 km depth (Banda et al., 1981). Note that recent study by Sagan et al. (2020) suggests the lithosphere beneath the island of Fuerteventura, southwest of Lanzarote, is perhaps more heterogenous with a mixture of both oceanic and continental lithosphere.

The easternmost and northernmost island of the archipelago is Lanzarote, at approximately 100 km from the coast of northwestern Africa (Figure 2.1a). Lanzarote's oldest surface volcanism is 15.5 Mya with the most recent eruption from the Timanfaya series in 1730 to 1736 and 1824 (Carracedo et al., 2012). Peridotite xenoliths, or blocks of upper mantle wall rock that are captured and brought to the surface by a host magma, are prominent in the Quaternary volcanic eruptions from Timanfaya (e.g., Fuster et al., 1968). Petrological and geochemical data of these peridotites offer a snapshot of the mantle composition, temperature, and pressure within the underlying mantle lithosphere.

Neumann et al. (1995) reports Lanzarote peridotite temperatures recalculated from CO_2 inclusions ranging from 870 to 1290°C, which results in a steep calculated geothermal gradient as >42°C/km. Based on this geothermal gradient, the mantle lithosphere beneath Lanzarote was thought to be thinner and hotter compared to the western islands (Neumann et al., 1995). This lithosphere thinning may be caused by thermal erosion from small scale convection due to the proximity of the continental edge (Vagnes and Amunderson, 1993; Neumann et al., 1995).

Petrology and geochemical work on Lanzarote peridotites have been previously studied by Siena et al. (1991), Neumann et al. (1995), Neumann and Wulff-Pedersen (1997) Neumann et al. (2004) and Bhanot et al. (2017). Most peridotites are spinel harzburgites (< 5% Cpx), with few spinel dunite and rare spinel lherzolite, lithologies. Forsterite contents in olivine range from 70 to 92, Al_2O_3 ranges from 0.1 to 3.0 wt. % in orthopyroxene, and spinel Cr# ranges from 27 up to 95 for samples bearing chromite (Siena et al., 1991, Neumann et al., 1995). Following batch modeling method by Niu (1997), Neumann et al. (2004) suggest Lanzarote peridotites have experienced 18 to 25% partial melting with the most refractory compositions ranging up to 30 to 32% partial melting.

The lithospheric mantle beneath the Canaries, as that is evidenced by the peridotite xenoliths, is thought to have experienced variable melt metasomatism with melt compositions that range from highly silicic to carbonatite at large (km) to small scale (m) distributions (Neumann et al., 2004). Neumann et al. (1995) suggests Lanzarote peridotites are both highly melt depleted as evidenced by rare earth element (REE) depletions in orthopyroxene, and depletions in heavy REEs (HREE) in clinopyroxene, and metasomatized by high Fe-Ti silicate melts and CO_2 fluid as evidenced by fluid inclusions, as well as enrichments of light REEs (LREE) in clinopyroxene. Siena et al. (1991) infers metasomatism by an alkali silicate melt with variable H_2O/H_2O+CO_2 fluid. The Sr isotopic compositions of peridotites xenoliths (Siena et al., 1991; with $^{87}Sr/^{86}Sr$ between 0.7031-0.7036) and the lavas (0.7029-0.7039) were explained by metasomatism of the oceanic lithosphere of presumably MORB source composition (e.g., $^{87}Sr/^{86}Sr$ <0.7025), by the Canaries mantle plume in the Neogene (Siena et al., 1991, Neumann et al., 1995), that possibly originates as carbonated pyroxenite from recycled oceanic crust (Gomez-Ulla et al., 2018). South of Lanzarote, the island of Fuerteventura has rare erupted oceanic carbonatites (e.g., Hoernle et al., 2002) thereby providing direct evidence for the presence of such melts within the Canaries plume. In addition, fracturing of the oceanic lithosphere due to its proximity to the ocean - continent transition may have also played a role in the movement of melts through the lithosphere (Neumann et al., 2004).

2.2 Sample selection

The studied peridotite samples were collected by Leslie Bruce as xenoliths from volcanic and cinder cone localities. Samples were selected from the Timanfaya volcanic fissure series eruption of 1730-1736, at cinder cone Montana Colorada, Caldera de los

Cuervos, and volcanic crater El Cuchillo (LBLZ23-, LBLZ27-, and LBLZ36-, respectively; Figure 2.1b). Peridotite LBLZ25-001 is from the beach of Salinas de Janubio and was likely transported from elsewhere on the island. From these localities, thirteen peridotite xenoliths were selected for geochemical (major, trace elements and water by FTIR) and petrographic analyses based on available material.

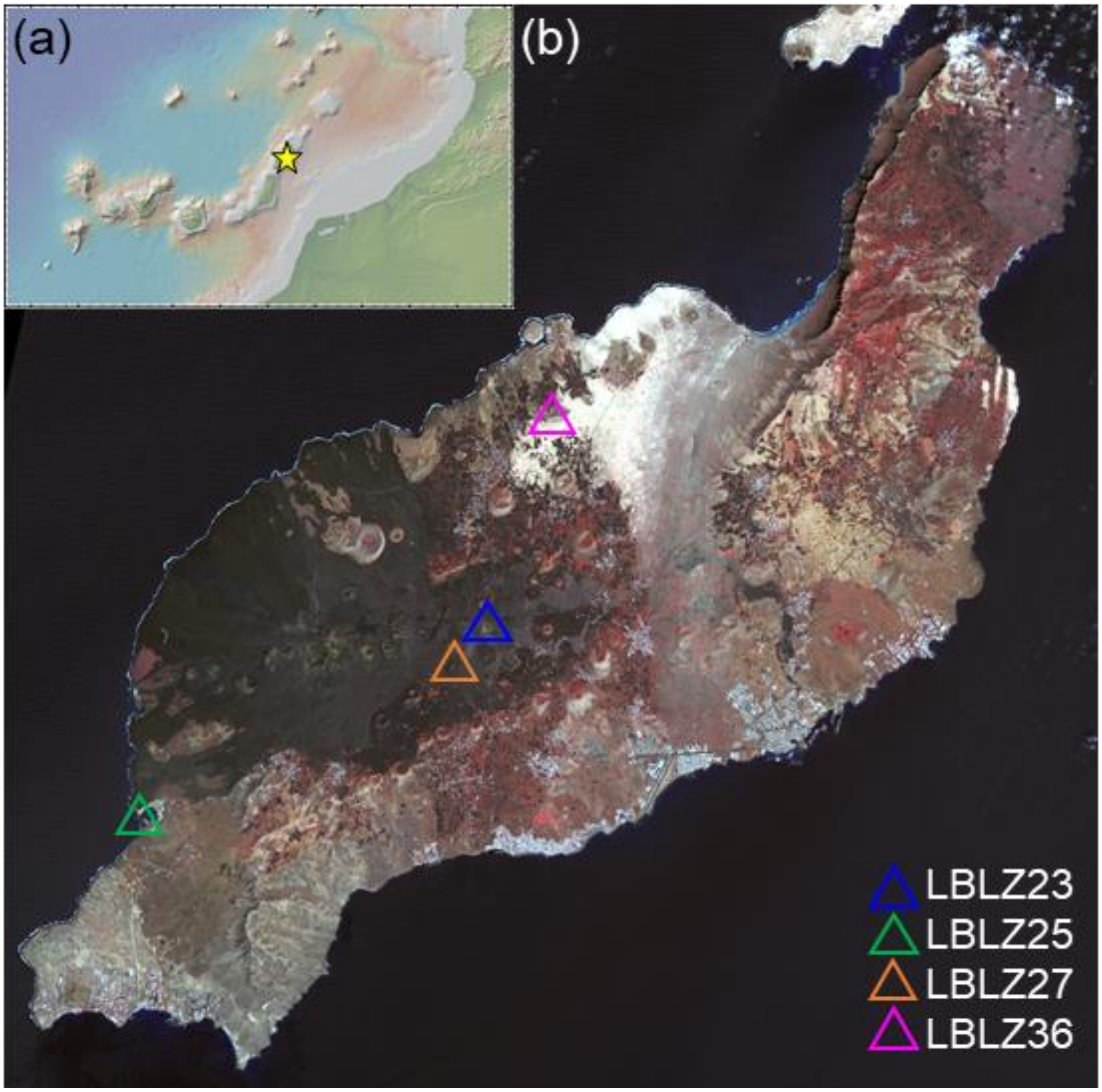

Figure 2.1. Location maps for Lanzarote and sampling sites. 2.1(a) Canary Islands location map showing the island of Lanzarote depicted by a yellow star. Map generated using GeoMapApp (Ryan et al., 2009). 2.1(b) Aerial image of Lanzarote edited to show sample location sites featured as triangles. Photo modified from NASA/METI/AIST/Japan Space Systems, and U.S./Japan ASTER Science Team.

CHAPTER 3

ANALYTICAL METHODS

3.1 Fourier Transform Infrared Spectroscopy (FTIR)

Olivine, orthopyroxene, and clinopyroxene were analyzed by FTIR for H_2O concentrations (Table 3.1). Procedures outlined from Peslier (2002), (2012), Peslier and Bizimis (2015), Bizimis and Peslier (2015), and Ashley et al. (2020) were followed. Peridotite xenoliths were disaggregated with an Al_2O_3 mortar and pestle then dry sieved. Silicate minerals were preconcentrated on a Frantz magnetic separator to make picking easier.

Mineral grains were carefully handpicked for minimal fractures and inclusions under a binocular microscope. Grains were mounted in epoxy, and doubly polished on two parallel sides with 1 µm alumina powder. When possible, grains were characterized based on their optical indicatrix orientations perpendicular to optic normal (ON), acute bisectrix (Bxa), or obtuse bisectrix (Bxo) and recorded. Individual grain thicknesses (200 to 1000 µm) were measured with a Mitutoyo digital micrometer (within ± 3 µm). Prior to FTIR analyses, mounts were placed for at least 1 hour in an 80°C oven to remove surface water.

Hydrogen was analyzed as hydroxyl using polarized infrared light spectra (in the range of 600 to 4500 cm^{-1}) on a Hyperion 3000 microscope linked to a Bruker Vertex 70

FTIR spectrometer, at the Astromaterials Research and Explorative Science (ARES) division of NASA-Johnson Space Center, Houston, Texas. Spectrometer and working area were continually flushed with nitrogen gas to limit atmospheric water. Aperture sizes ranged from 50 µm x 50 µm to 150 µm x 150 µm. Spectra resolution was 4 cm^{-1} for 128 scans. Background spectrum was measured every few mineral analyses. Analyses were completed in transmission mode with a mercury-cadmium-telluride (MCT) detector and a Zn-Se infrared polarizer with E parallel to predetermined refractive indices (α, β, or γ) based on the optical indicatrix orientation previously determined. Clinopyroxene was often ‘dirty’ with inclusions and limited such that these grains were measured with unpolarized infrared beam. Water concentrations for theses clinopyroxene grains were calculated following methods of Kovács et al. (2008) and Sambridge et al. (2008).

O-H infrared light absorbance bands were measured from 3700 to 3000 cm^{-1} for olivine and 3800 to 2800 cm^{-1} for pyroxenes with area baseline correction drawn by hand using the Thermo Omnic software. Spectra with serpentine (at ~3688 cm^{-1} bands, Libowitzky and Bean, 2004, Gose et al., 2011) and amphibole exsolutions in pyroxene (at ~3670 to 3700 cm -1; Sundvall and Stalder, 2011) were not included in the O-H vibration band absorbance areas, but also rarely observed. The average area absorbances were normalized to one cm grain thickness. A minimum of four grains per sample phase were measured at the most transparent and proximal to the grain core as possible.

H_2O ppm was calculated using a variation of the Beer-Lambert Law,

$$[\text{ppm } H_2O] = I' \, (A_\alpha + A_\beta + A_\gamma),$$

where $A_{(n)}$ is the integrated absorbance at each orientation (E‖α, E‖β, E‖γ) and I′ is the inverse of μ, the molar absorbance coefficient, with respect to thickness (normalized to 1 cm). We used I′ values of Si–H, 0.188 ± 0.012 for olivine, 0.0674 +/- 0.0027 (μ =14.84 ± 0.59) for orthopyroxene and 0.1410 ± 0.0064 (μ = 7.09 ± 0.32) for clinopyroxene (Bell et al., 1995; Bell et al., 2003). This method has approximately ± 20% uncertainty; calibration validity previously discussed elsewhere (Peslier et al., 2002; Bell et al., 2003; Mosenfelder and Rossman, 2013a, 2013b; Ashley et al., 2020).

3.2 Bulk rock XRF and EMP mineral major elements

Bulk rock (BR) major element data were collected for 12 peridotite xenoliths. Central interior fragments of the peridotites were selected, and any extraneous material and coatings were removed. At least 20 grams of sample were pulverized at University of South Carolina. Major element compositions were determined by X-Ray Florescence (XRF) at the Hamilton Analytical Laboratory, Hamilton College, New York. Mineral modal abundances were calculated by mass balance between the bulk rock data and measured mineral compositions by Electron microprobe. Bulk rock major elements, sample lithology, and modal abundances are shown in Table 3.2.

Major element concentrations of olivine, orthopyroxene, clinopyroxene, and spinel were determined by EMP analyses with a Cameca SX-100 Electron Microprobe in ARES, NASA-Johnson Space Center, TX and are reported in Table 3.3. An accelerating voltage of 15kV, beam currents of 20nA and counting times set to 20s and 10s on the peaks and backgrounds, respectively were used. Standards used were oligoclase (Na, Al), diopside (Si, Mg, Ca), forsterite (Si, Mg), chromite (Mg, Al, Cr, Fe), orthoclase (K), rutile (Ti), rhodonite (Mn), fayalite (Fe), and nickel oxide (Ni). Clean mineral grains were set in epoxy within plastic ring mounts, and progressively polished down to 1um with alumina powder on the operating side. On average a minimum of four points across the grain area were measured. Each data was checked for influence by inclusions, heterogeneities and exsolutions and discarded from the average sample mineral phase composition. Additional scanning electron microscope (SEM) electron backscatter images (BSE) captured spinel grains with spinel – pyroxene symplectites texture and melt pockets.

3.3 LA-ICPMS and solutions ICPMS trace elements

Ortho- and clinopyroxenes were selected for trace element analysis by laser ablation inductively coupled plasma mass spectrometry (LA-ICPMS). Pyroxene grains were analyzed using a Photon Machines Excimer 193 nm laser system coupled to an Element II high-resolution ICPMS system at the Center of Mass Spectrometry, University of South Carolina (CEMS, UofSC). Thirty-two elements were measured including rare earth elements (La, Ce, Pr, Nd, Sm, Eu, Gd, Tb, Dy, Ho, Er, Tm, Yb, Lu,) and Y, Sc, high field strength elements (Ti, Zr, Nb, Hf, Ta, Th, U), and other metals (Rb, Cs, Sr, Ba, V, Cr, Ni, Pb). Minerals were ablated following methods described in Frisby et al., (2016). A minimum of four grains per mineral phase from each sample were ablated at their cores. When possible, analyses were completed on the same grains used for major element collection. External calibration standards, NIST 612 and the United States Geological Survey (USGS) glasses BHVO-2G, BCR-2G and BIR-1G were used. Raw counts were converted to ppm concentrations using NIST 612 as external standard (Jochum et al., 2011; following Ashley et al., 2020) and using Si as internal standard with the concentrations for Si determined by EPM analyses. Few glass inclusions encompassed in spinel pyroxene composites were also ablated. Pyroxene and glass inclusion trace element concentrations are presented in Table 3.4.

Bulk rock trace element concentrations were determined by solution ICPMS at CEMS, UofSC. Approximately 50 mg of pulverized sample was spiked with a ^{145}Nd enriched spike. Spiked samples were dissolved in 3:1 HF:HNO_3 at ~100°C for at least three days, dried down, and repeatedly dried with 0.5 ml of concentrated Teflon-distilled HNO_3 to remove fluorides. Subsequently, samples were diluted with 100 mL of 2% HNO_3. The samples were analyzed on an ELEMENT2 HR-ICPMS. The ^{145}Nd/^{146}Nd ratio was used to determine the absolute Nd concentration of the sample, which then functioned as an internal standard. The USGS Georeferenced rock standard BHVO-2 was used as external standard. Multiple digestion-dissolutions of the international reference peridotite material UB-N were determined as unknowns. Averaged UB-N concentrations overlap well with values reported in the literature (Figure 3.2). Table 3.5 reports bulk rock and UB-N trace element concentrations.

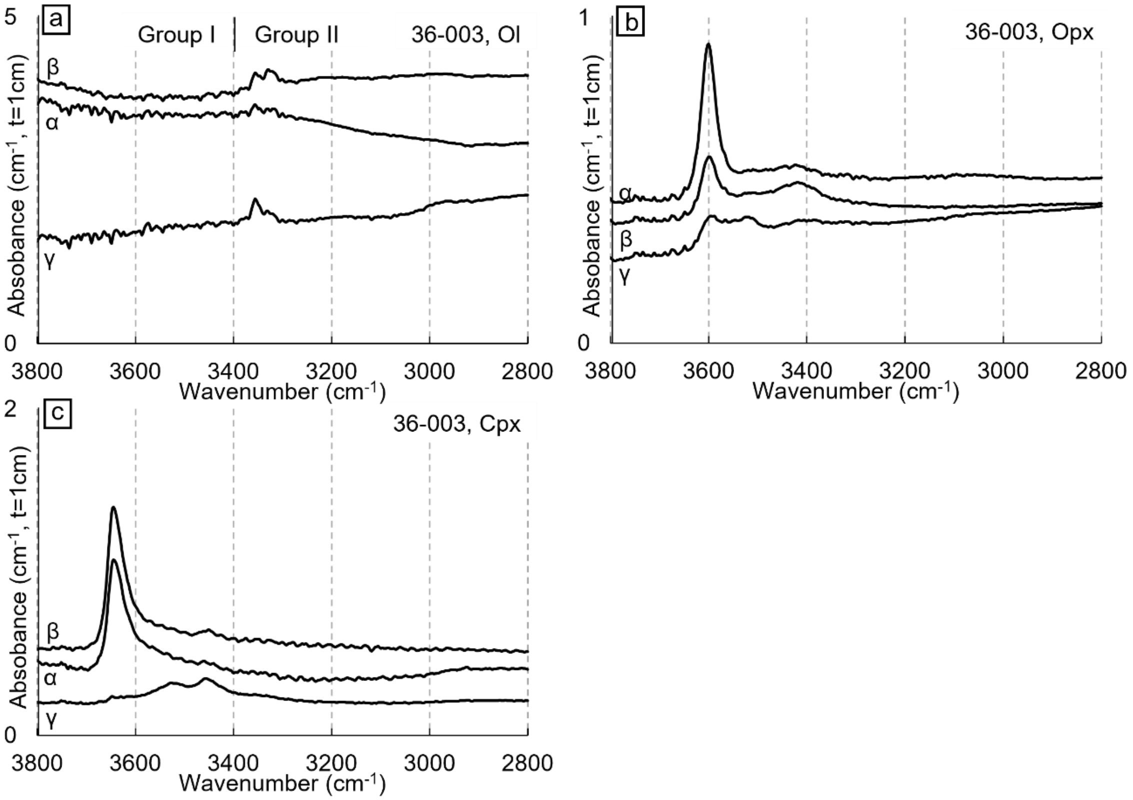

Figure 3.1. Representative polarized FTIR spectra of LBLZ36-003 (a) olivine, (b) orthopyroxene, and (c) clinopyroxene shown in the O-H region. Normalized to one centimeter thickness.

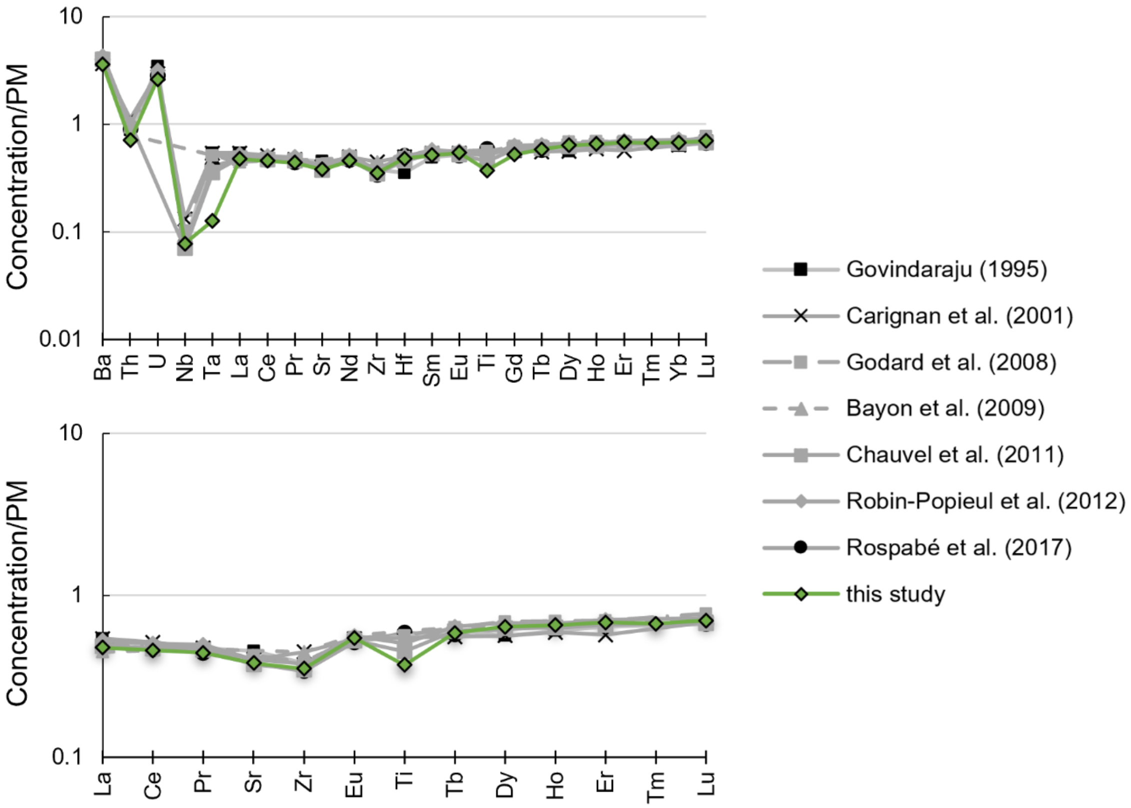

Figure 3.2. Averaged UB-N concentration (n=6) from this study. UB-N average values plotted with UB-N concentrations from literature for comparison and reproducibility (literature UB-N values from Rospabé et al., 2017 and sources therein). Values normalized to Primitive Mantle (PM) from McDonough and Sun (1995).

Table 3.1. Water concentrations of Lanzarote peridotites

	23-002	23-006	23-007	23-010	23-012	25-001
olivine						
H_2O ppm[1]	**11***	**15.1***	**2.7**	**4.3**	**4.1**	
1σ	2.4	3.7	0.4	0.7	0.7	
α	6	11	2	2	3	
β	extrap	extrap	2	3	1	
γ	extrap	extrap	3	3	4	
orthopyroxene						
H_2O ppm[2]	**99**	**67**	**80**	**88**	**42**	**58**
1σ	18	29	11	13	8	16
α	3	7	2	4	5	1
β	1	2	3	2	extrap	2
γ	3	9	3	6	5	3
clinopyroxene						
H_2O ppm[3]	**115**		**76***		**106***	
1σ	17		14		22	
α	1		extrap		extrap	
β	1		extrap		extrap	
γ	1		extrap		extrap	
bulk rock						
H_2O ppm	**34**	**33**[5]	**27**	**24**[5]	**22**	**24**[4,5]

	36-001	36-003	36-004	36-005	36-006	36-007
olivine						
H_2O ppm[1]	**8.2**	**6.8**	**6.1**	**8.4**	**7.0**	**8.1**
1σ	1.3	1	0.8	1.3	1.6	1.4
α	1	3	1	3	2	3
β	4	3	6	1	4	2
γ	10	4	6	4	4	3
orthopyroxene						
H_2O ppm[2]	**99**	**113**	**98**	**110**	**83**	**265**
1σ	19	23	12	13	9	25
α	4	1	2	6	4	1
β	5	2	3	1	1	3
γ	5	3	5	5	5	2
clinopyroxene						
H_2O ppm[3]	**251**	**258**		**274**		**470**
1σ	21	24		36		58
α	5	6		5		2
β	2	1		1		extrap
γ	7	5		4		2
Bulk rock						
H_2O ppm	**34**	**39**	**31**[5]	**52**	**28**[5]	**115**

Notes: * = unpolarized data acquired. [1] = Calculated using 0.188±0.012 (Bell et al., 2003); [2] = Calculated using 0.0674±0.027 for Opx and [3] = 0.141±0.006 for Cpx (Bell et al., 1995). When mineral water data was not collected for Ol ([5]) and Cpx ([6]), bulk rock water concentrations were reconstructed using estimations from mineral water partition coefficients. Abbreviations: bl = below limits; extrap = extrapolated; sample prefix = 'LBLZ-'.

Table 3.2. Bulk rock major element concentrations and mineral modal abundances

	23-002	23-006	23-007	23-010	23-012	25-001
Mineral modes						
Ol mode %	74	65.7	68.5	76.7	56.0	66.6
Opx mode%	24	33.2	29.9	23	40.4	29.3
Cpx mode%	1.5	0.5	1.1	0	2.7	2.9
Spl mode%	0.5	0.7	0.5	0.4	0.9	1.2
Bulk rock major element concentrations						
SiO_2		45.54	45.02	44.21	46.09	45.11
TiO_2		0.013	0.009	0.004	0.009	0.008
Al_2O_3		1.03	0.74	0.45	1.44	0.99
Cr_2O_3		0.70	0.53	0.33	0.75	0.54
FeO		7.23	7.71	7.88	7.24	7.77
MnO		0.13	0.13	0.13	0.13	0.13
MgO		44.69	45.30	46.62	43.09	44.37
NiO		0.28	0.29	0.31	0.26	0.27
CaO		0.65	0.61	0.37	1.01	0.82
Na_2O		0.04	0.04	0.00	0.04	0.08
K_2O		0.01	0.01	0.004	0.01	0.02
P_2O_5		0.01	0.00	0.004	0.01	0.01
LOI (%)		-0.51	-0.52	-0.54	-0.45	-0.48
total		99.58	99.68	99.63	99.42	99.44
Mg#		91.67	91.28	91.33	91.38	91.05
Cr#		31.47	32.30	32.76	25.94	26.96

	27-001	36-001	36-003	36-004	36-005	36-006	36-007
Mineral modes							
Ol mode %	78.9	73.8	76	71.6	62.1	70.9	59.3
Opx mode%	18.1	23.8	18	27.2	31.1	28	35.4
Cpx mode%	2.6	1.7	5	0	4.5	0	3.8
Spl mode%	0.4	0.7	1	1.2	2.3	1.1	1.5
Bulk rock major element concentrations							
SiO_2	43.60	44.16		44.46	44.67	44.39	46.06
TiO_2	0.005	0.019		0.007	0.009	0.033	0.021
Al_2O_3	0.39	0.94		0.76	1.43	0.80	1.10
Cr_2O_3	0.27	0.45		0.48	0.87	0.47	0.56
FeO	7.60	7.59		7.95	7.81	8.49	7.47
MnO	0.13	0.13		0.13	0.13	0.15	0.13
MgO	46.82	45.69		45.52	43.73	44.70	43.19
NiO	0.32	0.30		0.31	0.28	0.30	0.27
CaO	0.46	0.79		0.44	1.11	0.60	0.99
Na_2O	0.18	0.04		0.09	0.10	0.14	0.14
K_2O	0.05	0.01		0.02	0.03	0.04	0.04
P_2O_5	0.01	0.02		0.01	0.01	0.03	0.02
LOI (%)	-0.55	-0.50		-0.51	-0.43	-0.51	-0.32
total	99.44	99.47		99.45	99.49	99.44	99.46
Mg#	91.65	91.48		91.08	90.88	90.36	91.15
Cr#	31.14	24.19		29.89	28.96	28.18	25.47

Table 3.3. Major element data for Lanzarote peridotites

	23-002	23-006	23-007	23-010	23-012	25-001	27-001	36-001	36-003	36-004	36-005	36-006	36-007
Olivine													
SiO_2	40.81	40.71	40.74	41.04	39.32	40.75	40.72	40.53	40.66	40.76	40.09	40.41	41.09
TiO_2	0.010	0.004	0.006	0.008	0.090	0.010	0.006	0.006	0.006	0.004	0.011	0.007	0.018
Al_2O_3	0.057	0.026	0.040	0.013	0.030	0.019	0.019	0.032	0.020	0.024	0.026	0.030	0.047
Cr_2O_3	0.020	0.027	0.024	0.010	0.025	0.011	0.009	0.018	0.017	0.013	0.022	0.022	0.120
FeO	8.65	8.48	8.49	8.62	8.64	8.72	8.50	8.69	8.75	8.81	8.76	9.87	7.68
MnO	0.14	0.12	0.13	0.13	0.13	0.14	0.14	0.13	0.14	0.14	0.14	0.17	0.12
MgO	49.79	50.30	50.44	50.57	49.99	50.26	50.79	50.25	50.15	50.15	50.98	49.16	50.94
NiO	0.40	0.40	0.42	0.42	0.43	0.40	0.40	0.42	0.41	0.40	0.39	0.39	0.30
CaO	0.072	0.041	0.067	0.026	0.090	0.037	0.014	0.048	0.049	0.040	0.049	0.041	0.178
Na_2O	0.011	0.006	0.013	0.011	0.011	0.011	0.007	0.012	0.006	0.011	0.013	0.012	0.021
Total	99.97	100.12	100.35	100.85	98.68	100.36	100.60	100.14	100.20	100.36	100.49	100.11	100.49
Mg#[1]	91.11	91.35	91.37	91.27	91.17	91.12	91.41	91.15	91.08	91.02	91.21	89.87	92.20
Orthopyroxene													
SiO_2	55.66	55.75	55.12	55.51	55.73	56.13	56.65	56.01	55.77	56.24	56.05	56.30	56.01
TiO_2	0.007	0.012	0.011	0.012	0.007	0.011	0.008	0.010	0.009	0.008	0.008	0.027	0.011
Al_2O_3	2.42	2.18	2.16	1.93	2.24	1.98	1.25	2.53	2.51	2.00	2.31	1.71	2.12
Cr_2O_3	0.52	0.69	0.74	0.68	0.41	0.40	0.32	0.49	0.46	0.40	0.39	0.41	0.47
FeO	5.73	5.42	5.65	5.46	5.62	5.64	5.60	5.47	5.70	5.70	5.65	5.93	5.68
MnO	0.16	0.14	0.15	0.13	0.15	0.15	0.16	0.15	0.15	0.15	0.14	0.15	0.15
MgO	34.32	34.14	34.85	34.81	35.27	34.92	35.16	34.12	34.60	34.84	35.35	34.53	34.69
NiO	0.10	0.10	0.08	0.11	0.10	0.10	0.10	0.10	0.11	0.09	0.09	0.10	0.10
CaO	0.65	1.36	1.13	1.43	0.45	0.56	0.70	1.53	0.62	0.49	0.55	0.55	0.58
Na_2O	0.035	0.018	0.028	0.017	0.027	0.056	0.039	0.070	0.043	0.072	0.047	0.097	0.066
Total	99.59	99.81	99.91	100.07	99.99	99.95	99.99	100.47	99.97	100.00	100.59	99.80	99.87
Mg#	91.43	91.83	91.67	91.91	91.79	91.66	91.80	91.73	91.54	91.59	91.77	91.20	91.58

	23-002	23-006	23-007	23-010	23-012	25-001	27-001	36-001	36-003	36-004	36-005	36-006	36-007
Clinopyroxene													
SiO_2	53.08	52.95	53.27	53.02	52.68	53.64	52.81	52.78	52.91		52.82		53.17
TiO_2	0.0230	0.0749	0.0668	0	0.0200	0.0320	0.0233	0.0248	0.0134		0.0172		0.0494
Al_2O_3	2.69	2.62	2.29	1.45	2.29	1.97	3.02	2.52	2.90		2.62		2.06
Cr_2O_3	0.83	0.89	1.13	1.02	0.62	0.48	2.96	0.67	0.77		0.68		1.64
FeO	2.79	2.69	3.28	2.76	2.39	2.35	2.86	2.51	2.55		2.48		2.69
MnO	0.09	0.09	0.10	0.08	0.08	0.08	0.09	0.08	0.08		0.09		0.09
MgO	18.04	18.80	19.67	19.84	17.72	17.27	16.88	17.66	17.13		17.47		18.20
NiO	0.05	0.06	0.06	0.06	0.05	0.04	0.06	0.06	0.05		0.04		0.04
CaO	21.07	20.89	18.78	20.69	22.64	22.37	18.62	21.95	21.88		21.89		20.82
Na_2O	0.50	0.24	0.47	0.18	0.61	0.75	1.65	0.77	0.71		0.86		0.53
Total	99.16	99.31	99.11	99.09	99.08	98.97	98.99	99.02	99.00		98.96		99.30
Mg#	92.03	92.58	91.45	92.77	92.97	92.90	91.29	92.62	92.28		92.62		92.36
T*	1069	1113	1088	1153	861			960	964	893	914	919	1086
μ**	9E+21	3E+21	4E+21	7E+21	1E+26			2E+24	6E+23	1E+25	6E+24	3E+24	1E+22
Spinel													
SiO_2	0.080	0.023	0.072	0.049	0.095	0.022	0.005	0.103	0.032	0.021	0.060	0.030	0.095
TiO_2	0.025	0.014	0.755	0.009	0.030	0.100	0.027	0.055	0.015	0.051	0.020	0.597	0.064
Al_2O_3	30.18	25.85	20.06	24.21	31.24	24.75	12.40	30.73	33.37	21.50	32.10	16.32	17.80
Cr_2O_3	36.89	41.60	46.98	45.21	35.77	39.75	48.45	36.07	32.22	44.22	34.28	47.37	47.66
FeO	15.50	15.70	17.48	15.27	15.64	19.48	24.78	16.35	17.29	18.40	16.33	21.95	18.13
MnO	0.15	0.18	0.16	0.19	0.15	0.26	0.26	0.18	0.17	0.19	0.14	0.27	0.23
MgO	17.04	16.13	15.02	0.12	17.60	15.63	13.50	16.92	16.61	15.62	17.36	13.51	15.64
NiO	0.25	0.15	0.16	0.12	0.23	0.19	0.19	0.21	0.22	0.18	0.23	0.15	0.18
CaO	0.014	0.010	0.017	0.006	0.007	0.012	0.009	0.028	0.009	0.011	0.029	0.012	0.034
Na_2O			0.021	0.018	0.017			0.014			0.019		0.016
Total	100.13	99.66	100.61	100.38	100.77	100.17	99.62	100.65	99.95	100.19	100.55	100.21	99.84
Mg#	66.20	64.68	60.52	64.12	66.73	58.76	49.26	64.84	63.12	60.21	65.46	52.31	60.59
Cr#[2]	45.07	51.92	61.13	55.27	43.44	51.97	72.40	44.05	39.32	58.00	41.75	66.09	64.25
F (%)[3]	16.0	17.4	19.1	18.1	15.7	17.5	20.8	15.8	14.7	18.6	15.3	19.9	19.6
F (%)[4]		17.9	19.9	21.9	15.0	18.1	22.4	18.4		19.8	15.1	19.5	17.3

	36-004	36-006
Glass Inclusions		
SiO_2	60.46	54.59
TiO_2	0.17	1.30
Al_2O_3	17.52	14.95
Cr_2O_3	0.07	0.41
FeO	3.43	5.83
MnO	0.05	0.11
MgO	4.13	6.94
NiO	0	0.03
CaO	8.02	10.26
Na_2O	4.49	3.77
Total	98.34	98.19

Notes: (1) Mg# = [100*Mg / (Mg+Fe)]; (2) Cr# = [100*Cr / (Cr+Al)]; (3) F (%) estimations calculated following methods in Hellebrand et al. (2001); (4) = F (%) estimations calculated following methods in Canil et al. (2002); * = equilibration temperatures calculated following methods in Brey and Kohler (1990); ** = viscosity estimates following methods in Peslier et al. (2010).

Table 3.4. Trace element concentrations for orthopyroxene, clinopyroxene, and glass inclusions from Lanzarote peridotites

	23-002 Opx	23-006 Opx	23-007 Opx	23-010 Opx	23-012 Opx	25-001 Opx	36-001 Opx
Sc	24	26	22	24	21	20	20
Ti	34	19	7	10	34	26	35
V	91	91	67	73	46	76	51
Cr	5036	5341	3903	4622	62351	4910	62693
Ni	718	718	603	750	7891	738	8274
Rb	0.076	0.031	0.042	0.007	0.008	0.091	0.004
Sr	8.0	0.1	1.1	0.02	0.9	12.6	0.3
Y	0.15	0.06	0.03	0.10	0.08	0.31	0.28
Zr	0.05	bdl	0.05	0.01	0.04	1.22	2.40
Nb	0.07	0.02	0.01	0.01	0.02	0.10	0.06
Cs	0.003	0.005	0.001	0.002	0.0002	0.003	0.0002
Ba	0.10	0.29	0.42	0.02	0.02	0.47	0.004
La	0.36	0.01	0.01	0.0003	0.04	0.76	0.01
Ce	0.85	0.01	0.03	0.001	0.09	1.32	0.05
Pr	0.09	0.000	0.003	0.000	0.01	0.10	0.01
Nd	0.32	0.002	0.01	0.001	0.03	0.29	0.05
Sm	0.05	bdl	0.003	0.001	0.002	0.04	0.02
Eu	0.012	0.0005	0.002	0.0004	0.002	0.013	0.010
Gd	0.032	0.002	0.008	0.002	0.008	0.042	0.036
Tb	0.003	0.0005	0.001	0.001	0.001	0.007	0.006
Dy	0.019	0.005	0.006	0.007	0.005	0.041	0.041
Ho	0.004	0.002	0.001	0.003	0.002	0.010	0.009
Er	0.020	0.011	0.004	0.019	0.011	0.035	0.032
Tm	0.004	0.004	0.001	0.005	0.003	0.008	0.005
Yb	0.051	0.044	0.021	0.059	0.032	0.062	0.043
Lu	0.011	0.011	0.005	0.012	0.007	0.014	0.008
Hf	0.0004	0.002	0.002	0.0002	0.0003	0.004	0.027
Ta	0.001	0.0004	0.001	0.0001	0.001	0.004	0.009
Pb	0.033	0.191	0.030	0.023	0.008	0.066	0.026
Th	0.166	0.0002	0.001	0.0002	0.019	0.491	0.002
U	0.035	0.0002	0.001	bdl	0.006	0.069	0.001

	36-003 Opx	36-004 Opx	36-005 Opx	36-006 Opx	36-007 Opx	23-002 Cpx	23-006 Cpx
Sc	18	14	21	12	14	79	46
Ti	10	26	14	123	13	53	294
V	80	67	62	48	79	188	154
Cr	3277	2686	48715	3185	3825	7438	6081
Ni	781	739	8104	760	716	393	496
Rb	0.182	0.134	0.003	0.114	0.150	0.048	0.204
Sr	1.8	0.3	0.4	0.6	1.1	183.8	11.0
Y	0.08	0.35	0.06	0.64	0.33	2.86	1.16
Zr	0.24	1.64	0.04	3.18	0.44	0.32	3.02
Nb	0.10	0.03	0.04	0.07	0.04	0.09	0.30
Cs	0.004	0.003	0.0001	0.01	0.003	0.003	0.01
Ba	0.02	0.02	0.004	0.11	0.03	3.76	2.68
La	0.10	0.01	0.01	0.03	0.05	7.10	0.43
Ce	0.15	0.06	0.05	0.10	0.18	19.10	1.16
Pr	0.01	0.01	0.01	0.02	0.02	2.30	0.16
Nd	0.04	0.06	0.03	0.10	0.08	8.73	0.77
Sm	0.01	0.02	0.00	0.05	0.02	1.43	0.22
Eu	0.004	0.011	0.002	0.020	0.009	0.402	0.086
Gd	0.013	0.034	0.018	0.071	0.018	0.969	0.256
Tb	0.001	0.007	0.001	0.015	0.006	0.112	0.038
Dy	0.008	0.052	0.004	0.106	0.037	0.533	0.222
Ho	0.002	0.012	0.001	0.023	0.010	0.098	0.044
Er	0.011	0.040	0.007	0.077	0.040	0.283	0.141
Tm	0.003	0.007	0.002	0.012	0.009	0.044	0.024
Yb	0.039	0.072	0.022	0.111	0.075	0.309	0.199
Lu	0.009	0.012	0.006	0.020	0.014	0.055	0.037
Hf	0.002	0.015	bdl	0.048	0.001	0.003	0.097
Ta	0.005	0.001	0.0005	0.004	0.0005	0.0004	0.021
Pb	0.273	0.063	0.001	0.051	0.094	1.241	0.544
Th	0.048	0.008	0.003	0.008	0.053	0.447	0.025
U	0.015	0.002	0.003	0.003	0.006	0.147	0.008

	23-007	23-012	25-001	27-001	36-001	36-003	36-005
	Cpx	Cpx	Cpx	Cpx	Cpx	Cpx	Cpx
Sc	78	78	73	117	69	69	69
Ti	827	74	74	172	120	21	46
V	201	135	147	236	157	193	191
Cr	10472	3478	3746	16411	3930	5503	3688
Ni	554	362	349	351	422	376	383
Rb	0.065	0.057	0.059	3.177	0.040	0.024	0.018
Sr	29.5	263	466	481	210	318	258
Y	2.27	1.57	4.01	24.77	4.10	1.23	1.86
Zr	4.53	0.77	14.80	32.8	28.79	4.16	8.44
Nb	0.10	0.10	0.07	21.95	0.37	0.65	bdl
Cs	bdl	bdl	0.01	0.20	bdl	0.004	bdl
Ba	0.29	1.05	23.22	18.68	0.25	0.11	0.11
La	0.60	16.62	27.76	11.18	9.6	15.3	12.6
Ce	1.90	24.40	51.53	39.45	24.7	20.3	26.5
Pr	0.20	bdl	4.16	6.64	2.8	1.6	2.5
Nd	1.90	5.69	11.58	33.33	11.6	4.8	8.0
Sm	0.59	0.58	1.52	8.76	2.13	0.59	1.03
Eu	0.204	0.147	0.450	2.990	0.644	0.198	0.301
Gd	0.608	0.435	1.109	7.691	1.581	0.362	0.835
Tb	bdl	bdl	0.148	1.162	bdl	0.039	bdl
Dy	0.531	0.232	0.799	5.753	0.936	0.198	0.369
Ho	0.091	0.053	0.142	0.990	0.157	0.045	0.069
Er	0.237	0.199	0.396	2.337	0.400	0.166	0.196
Tm	bdl	bdl	0.059	0.285	0.053	0.031	0.030
Yb	0.237	0.317	0.388	1.730	0.379	0.247	0.251
Lu	0.038	0.053	0.064	0.217	0.056	0.046	0.039
Hf	0.177	0.005	0.103	0.432	0.432	0.027	0.101
Ta	0.008	0.003	0.004	0.521	0.091	0.071	bdl
Pb	2.327	2.607	1.710	0.476	3.241	1.058	1.664
Th	0.049	1.367	2.030	0.220	0.669	1.710	1.051
U	0.010	0.380	0.393	0.059	0.179	0.394	0.326

	36-007 Cpx	27-001 incl*	36-004 incl*	36-006 incl*
Sc	80	41	47	48
Ti	131	194	4289	8023
V	178	470	271	307
Cr	8147	755	1433	7070
Ni	418	65	155	120
Rb	0.266	81	12	20
Sr	451	843	714	810
Y	13.8	20.8	17.3	19
Zr	45.24	56.9	266	286
Nb	1.74	237	121	126
Cs	0.002	1.24	0.03	0.11
Ba	16.46	808	189	272
La	13.7	24.2	21.2	28.8
Ce	44.9	74.7	66.5	79.2
Pr	5.9	9.7	9.2	10.4
Nd	25.5	40.3	40.3	44.6
Sm	5.42	8.40	8.42	8.87
Eu	1.824	2.77	2.68	2.98
Gd	4.436	6.05	6.07	6.94
Tb	0.583	0.92	0.87	0.97
Dy	3.045	4.65	4.14	4.56
Ho	0.496	0.79	0.67	0.75
Er	1.216	1.93	1.64	1.79
Tm	0.150	0.25	0.19	0.21
Yb	0.880	1.52	1.11	1.39
Lu	0.123	0.20	0.15	0.17
Hf	0.437	0.40	4.27	5.24
Ta	0.094	3.37	5.30	5.80
Pb	1.038	3.84	1.75	2.39
Th	0.457	1.34	0.74	1.54
U	0.128	0.44	0.21	0.45

Notes: * = glass inclusion; sample prefix = ‘LBLZ-’

Table 3.5. Bulk rock and UB-N trace element concentrations for Lanzarote peridotites

	23-006	23-007	23-010	23-012	25-001
	BR	BR	BR	BR	BR
Sc	10	10	8	12	10
Ti	53	23	4	30	25
V	35	27	22	36	32
Cr	2853	2019	1725	3747	2203
Ni	2404	2519	2854	2077	2177
Rb	0.08	0.09	0.01	0.05	0.26
Sr	1.83	3.16	0.31	13.58	33.02
Y	0.11	0.05	0.11	0.14	0.31
Zr	0.83	0.32	0.15	0.43	3.79
Nb	0.14	0.07	0.02	0.13	0.46
Cs	0.004	0.003	0.001	0.002	0.003
Ba	0.91	0.97	0.19	2.20	10.38
La	0.11	0.06	0.01	0.85	1.92
Ce	0.22	0.12	0.03	1.22	2.98
Pr	0.03	0.01	0.00	0.10	0.25
Nd	0.11	0.05	0.01	0.29	0.74
Sm	0.024	0.012	0.002	0.032	0.095
Eu	0.008	0.004	0.001	0.011	0.032
Gd	0.027	0.012	0.003	0.049	0.133
Tb	0.004	0.002	0.001	0.004	0.013
Dy	0.020	0.009	0.010	0.019	0.058
Ho	0.004	0.002	0.004	0.005	0.012
Er	0.013	0.006	0.016	0.018	0.034
Tm	0.003	0.001	0.004	0.004	0.005
Yb	0.022	0.012	0.036	0.036	0.042
Lu	0.005	0.003	0.007	0.008	0.008
Hf	0.021	0.007	0.004	0.008	0.065
Ta	0.009	0.004	0.001	0.004	0.012
Pb	0.073	0.064	0.028	0.084	0.099
Th	0.010	0.005	0.002	0.183	0.239
U	0.003	0.002	0.001	0.047	0.048

	27-001 BR	36-001 BR	36-004 BR	36-005 BR	36-006 BR
Sc	6	8	8	11	8
Ti	8	90	25	26	159
V	16	26	27	52	22
Cr	937	2616	1852	4573	1621
Ni	2461	2521	2643	2316	2525
Rb	0.62	0.24	0.23	0.11	0.32
Sr	27.83	12.01	20.83	17.88	18.93
Y	1.39	0.34	0.48	0.12	1.03
Zr	2.78	3.78	3.83	0.68	12.08
Nb	4.97	0.49	1.49	0.23	3.58
Cs	0.010	0.006	0.002	0.003	0.002
Ba	5.75	3.78	6.15	2.99	6.12
La	1.21	0.73	0.83	0.96	0.63
Ce	3.05	1.45	1.78	1.67	1.98
Pr	0.42	0.16	0.22	0.15	0.30
Nd	1.81	0.62	0.87	0.44	1.40
Sm	0.418	0.113	0.173	0.047	0.344
Eu	0.139	0.037	0.054	0.014	0.110
Gd	0.412	0.121	0.170	0.069	0.320
Tb	0.059	0.015	0.021	0.005	0.045
Dy	0.306	0.068	0.099	0.021	0.226
Ho	0.054	0.012	0.017	0.004	0.040
Er	0.136	0.034	0.047	0.015	0.101
Tm	0.018	0.005	0.007	0.003	0.014
Yb	0.116	0.039	0.047	0.026	0.095
Lu	0.017	0.007	0.008	0.005	0.015
Hf	0.030	0.083	0.050	0.014	0.186
Ta	0.113	0.037	0.054	0.011	0.208
Pb	0.122	0.054	0.065	0.070	0.051
Th	0.140	0.094	0.076	0.140	0.025
U	0.035	0.024	0.019	0.038	0.007

	36-007 BR	UB-N	UB-N 1σ
Sc	9	13.2	0.55
Ti	71	446	146
V	27	63.9	2.7
Cr	1790	2475	157
Ni	1720	2013	114
Rb	0.33	3.3	0.23
Sr	25.00	7.6	0.4
Y	0.89	2.6	0.14
Zr	4.69	3.7	0.3
Nb	1.38	0.051	0.006
Cs	0.003	12.2	0.9
Ba	6.01	23.8	2.1
La	1.09	0.308	0.02
Ce	2.62	0.768	0.05
Pr	0.34	0.112	0.008
Nd	1.44	0.572	0.036
Sm	0.307	0.209	0.012
Eu	0.102	0.084	0.004
Gd	0.301	0.285	0.018
Tb	0.040	0.058	0.004
Dy	0.191	0.430	0.023
Ho	0.033	0.098	0.005
Er	0.083	0.299	0.016
Tm	0.011	0.045	0.003
Yb	0.075	0.300	0.018
Lu	0.012	0.047	0.003
Hf	0.069	0.136	0.011
Ta	0.055	0.005	0.001
Pb	0.064	11.871	2.274
Th	0.082	0.057	0.006
U	0.020	0.053	0.005

Notes: Standard deviation of the averaged UB-N (n=6) concentrations = 1σ; sample prefix = ‘LBLZ-’

CHAPTER 4

RESULTS

4.1 Petrography

The xenoliths range from a few centimeters up to 12 centimeters. The xenoliths are commonly a teardrop shape, perhaps an effect from deformation or ablation from the magma upon ascent to the surface (Figure 4.1). Peridotite mineral modal compositions calculated by mass balance are reported in Table 3.2. The Lanzarote peridotites are primarily spinel-harzburgites (Figure 4.2) with average mineral modes of 69.2 vol. % for Ol, 27.8 vol. % for Opx, 2.0 vol. % for Cpx, and 0.9 vol.% for Spl. Hydrous alteration phases such as amphibole and phlogopite were not observed. Petrographic descriptions are reported below.

Lanzarote peridotites petrographic observations are consistent with previous descriptions (e.g., Siena et al., 1991; Neumann et al., 1995; 2002; 2004). Olivine and orthopyroxene grain sizes range from less than 0.1 mm up to 5 mm, with clinopyroxene and spinel grains ≤0.5 mm. The peridotites have protogranular and porphyroclastic textures (Figure 4.3a, 4.3b; respectively) with some deformational features. Porphyroclastic olivine grains often show kink banding (Figure 4.3a). LBLZ23-010 has striated olivine (Figure 4.3c; LBLZ23-010). Orthopyroxenes often have exsolutions of clinopyroxene and spinel. A few samples show exsolved orthopyroxene disjointed by kink bands suggesting that the deformation occurred after the exsolutions. Clinopyroxenes are typically found in proximity to spinel grains and vary in mineral clarity. Some spinels exhibit vermicular textures with equigranular sponge-like rims (e.g., Figures 4.3d, 4.4). Fluid inclusions and fractures were minimally present in all samples, particularly in olivine and orthopyroxene.

Second generation mineral assemblages are less deformed, if at all, and are found as protogranular clusters of neoblasts of olivine, orthopyroxene, and clinopyroxene that are typically interstitial with vermicular spinel. These clusters are typically encompassed by larger (1-2mm) primary grains (Figure 4.3e). Approximately half the samples show these spinel symplectite composites and locally higher concentration of clinopyroxenes than throughout the rest of the sample. LBLZ36-004 shows an example of these clusters of fine-grained mineral aggregates with glass surrounding spinel in an otherwise protogranular texture, suggesting either partial melting or melt infiltration (Figure 4.3e). Primary grain boundaries surrounding these spinel composites are typically irregular and jagged with the silicate aggregates having clean and rounded boundaries. Approximately half the samples show needles of plagioclase near and around spinel pyroxene clusters ± glass. Some samples have vermicular spinel with secondary mineral aggregates in a glass matrix most likely indicative of a fluid or melt exsolving at the junction of once primary minerals and spinel.

4.2 Major element compositions

Lanzarote peridotite olivine Mg# [100*(Mg+Fe)/Mg] ranges from 89.9 to 92.2, orthopyroxene from 91.2 to 91.9, and for clinopyroxene 91.3 to 93.0. Figure 4.4(a-b) shows positive correlations between silicate mineral Mg#, suggesting that the minerals in these peridotites are generally in equilibrium. LBLZ36-006 has the lowest olivine Mg# (89.9) in an apparent disequilibrium with the orthopyroxene (no data available for clinopyroxene). In contrast, LBLZ36-007 with the highest olivine Mg# (92.2) is also in disequilibrium between olivine and pyroxenes. Nonetheless, most mineral Mg# overlap well with compositions of abyssal peridotites and other oceanic island peridotites (Fig. 4.4).

The low mineral and bulk rock Al_2O_3 contents and high spinel Cr# [100*(Cr+Al)/Cr; excluding grains with >0.1 wt.% TiO_2 contents] overlap with the most melt depleted oceanic peridotites (Figure 4.4c-e). However, five peridotites have higher bulk rock Al_2O_3 contents for a given spinel Cr# (arrow in Figure 4.4e), possibly indicative of melt infiltration and addition of Al to the rock, but not spinel.

The spinels have Cr# from 39.3 to 72.4 and Mg# from 49.3 to 66.7 (Figure 4.4f). Using the spinel Cr# as a proxy for extent of melting (after Hellebrand et al. 2001), and only for spinels with <0.1 wt.% TiO2 content (to avoid the possible effects of metasomatism on the calculation) Lanzarote peridotites show high estimates for degree of melt depletion; 15 to 21%. Notably, some spinels show complex core-to-rim compositional differences, with enrichments in TiO_2 and depletions in Al_2O_3 at grain rims, and variable Cr_2O_3 contents (Figure 4.5 and associated Table 4.1). Spinel TiO_2 contents range from trace up to 0.8 wt. % in spinel grain cores and some samples have very high titanium contents at their rims (e.g., up to 3.3 wt. %, LBLZ25-001).

The modal composition of clinopyroxene compared to spinel Cr# is consistent with extensive partial melting as with increasing degree of melting clinopyroxene is increasingly removed from the residue (Figure 4.6b; Dick and Bullen, 1984, Kinzler and Grove 1992).

However, there are a few peridotites that have higher modal clinopyroxene for their melting estimates, perhaps suggesting secondary clinopyroxene formation from melt addition. Clinopyroxene Na_2O contents are high for a given spinel Cr# (Figure 4.6a), also consistent with Na addition to the peridotite.

A few glass inclusions were measured for their major element compositions (Table 3.3). These glasses have variable but high SiO_2 and moderate to low TiO_2 contents (SiO_2: 55-61 wt.%, TiO_2: 0.2-1.3 wt.%, Al_2O_3: 15-18 wt.%, MgO: 4-7 wt.%, CaO: 8-10 wt.%). These data are consistent with previous studies (Neumann and Wulff-Pederson 1997) who reported a wide range in glass compositions in Lanzarote peridotites with SiO_2 contents ranging from 55-73 wt.% SiO_2 and up to 1.3 wt.% TiO_2.

The calculated equilibration temperatures for the Lanzarote peridotites range from 861 to 1113°C (calculations using CaO contents of the orthopyroxene after Brey and Kohler, 1990; see Table 3.3). Temperatures are on average a 100°C higher for Montana Colorada peridotites than El Cuchillo (LBLZ23-, 1056°C; LBLZ36-, 956°C; respectively).

4.3 Trace element concentrations

Lanzarote pyroxenes and bulk rocks show variable rare earth element (REE) enrichments and depletions with complexities that are indicative of both melt depletion and metasomatism. Bulk rock REE concentrations range approximately two orders of magnitude below primitive mantle and most samples have negative Zr, Hf, and Ti anomalies with respect to the adjacent elements in a compatibility plot (spider gram) (Figure 4.7a). Orthopyroxenes show a large range in LREE concentrations that vary up to four orders of magnitude (Figure 4.7b), while the HREE tend to converge to within one order magnitude range. Some samples have positive Sr anomalies and some have high $(Zr/Hf)_{PM}$ ratios, negative Ti anomalies and thus low $(Ti/Eu)_{PM}$ ratios ($[Zr/Hf]_{PM}$ = up to 18.7, $(Ti/Eu)_{PM} \leq 0.2$). Most clinopyroxenes have enrichments of LREE (Figure 4.7c) over HREE and high $(Zr/Hf)_{PM}$, and low $(Ti/Eu)_{PM}$ (up to 4.2, ≤ 0.007; respectively). However, LBLZ23-006 and LBLZ23-007 have clinopyroxenes with relatively flat REE profiles, similar to the primitive mantle.

Despite the large variance, the pyroxene and bulk rock trace element systematics show some distinct patterns and can be separated into three groups (Group I, II, and III). In Figure 4.8a, both the bulk rock and orthopyroxene LREE are depleted relative to the HREE and with a positive Ti anomaly in the orthopyroxene. Three other peridotites show relatively flat REE profiles (Figure 4.8b-c; LBLZ23-006, LBLZ23-007, LBLZ36-006). Specifically, LBLZ23-007 bulk rock and orthopyroxene have REE lower than primitive mantle and clinopyroxene that closely parallels primitive mantle composition with small negative Ti and Zr anomalies, also present in the corresponding orthopyroxene (Figure 4.8c). The peridotite with the most LREE depleted patterns and the three peridotites with relatively flat REE profiles are grouped together as Group I.

The rest of the Lanzarote peridotites have trace element compositions similar to that of carbonatites found on Fuerteventura (Figure 4.9). These peridotites have bulk rock and pyroxene trace element concentrations with high La/Yb and Zr/Hf ratios as well as low Ti/Eu ratios which are more distinguished in the clinopyroxenes. We define these peridotites as Group II.

LBLZ36-001 has clinopyroxene with high La/Yb and Zr/Hf ratios as well as low Ti/Eu ratios mirroring that of carbonatites (Figure 4.10). Yet the bulk rock concentrations only exhibit slight LREE enrichments and a relatively flat profile. Also, the orthopyroxene is LREEs depleted with a strong Zr positive anomaly. Due to the compositional differences between the bulk rock and pyroxenes we call this Group III.

Lanzarote peridotite trace element compositions also appear to vary by location-site (Figure 4.11). The peridotites from El Cuchillo typically have enrichments in LREE over HREE and strong negative Hf, Ti, and Zr anomalies in the bulk rock and clinopyroxenes. The Montana Colorada peridotites have lower bulk rock trace element concentrations than El Cuchillo and a wider range of LREE concentrations with only one sample having negative Hf, Zr, Ti anomalies. All of El Cuchillo and half of the Montana Colorada samples have clinopyroxene trace element concentrations with high La/Yb, low Ti/Eu ratios and high Zr/Hf ratios (average: $(La/Yb)_{PM}$ =26±13, $(Ti/Eu)_{PM}$ =0.02±0.02, $(Zr/Hf)_{PM}$ =2.9±1; respectively), characteristic of carbonatite melt compositions. However, two samples from Montana Colorada have clinopyroxenes with relatively flat profiles, similar to that of the primitive mantle.

Trace elements of glass inclusions were measured from three peridotites (see Table 3.5). The glass inclusions have two unique trace element compositions, but all are enriched in LREE/HREE with high $(La/Yb)_{PM}$ ratios (up to 14; Figure 12). All measured glass has negative Zr, Hf, and Ti anomalies but the inclusions in sample LBLZ27-001 are similar to its clinopyroxene ($[Ti/Eu]_{PM}$ = 0.009, $(Zr/Hf)_{PM}$ =11; LBLZ27-001).

4.4 Water concentrations

Representative FTIR spectra of Lanzarote peridotites NAMs are shown in Figure 3.1. FTIR Spectra of olivines show OH absorbance peaks on 3571 and 3527 for Group I, and 3355 and 3330 for Group II bands. Orthopyroxenes have OH absorbance peaks typically at 3600 for α β and ~3500 for γ orientations. For clinopyroxenes OH absorbance peaks are at ~3620 band.

Water concentrations of NAMs (Ol, Opx, Cpx) in Lanzarote peridotites cover the full range of other reported oceanic peridotite water contents (e.g., Warren and Hauri, 2014; Peslier et al., 2015; Schaffer at al., 2019; Ashley et al., 2020; Zhang et al., 2020). Lanzarote olivine H_2O contents (7.1 ± 3.4 ppm) range from the lowest reported (e.g., Savai'i, Samoa; Ashley et al., 2020) to highest contents (e.g., abyssal peridotites, Warren and Hauri, 2014). Pyroxenes have higher water contents ranging from 42.2 to 265 ppm and 75.7 to 470 ppm (Opx, Cpx; respectively). The apparent water partition coefficient between olivine and orthopyroxene ($D_{H2O}^{Ol/Opx} = 0.08 \pm 0.05$) is within the range of other mantle samples ($D_{H2O}^{Ol/Opx} = 0.11 \pm 0.10$; Warren and Hauri, 2014; Figure 4.13a). Sample LBLZ36-007 shows disequilibrium between olivine and orthopyroxene water concentrations with very low water in olivine for the water content in orthopyroxene. Lanzarote apparent water partition coefficient between clinopyroxene and orthopyroxene is within that reported in the literature ($D_{H2O}^{Cpx/Opx} = 2.0 \pm 0.7$; 1:2-2.5; respectively; Figure 4.13b).

Recalculated peridotite bulk rock water contents range from 22 to 115 ppm with an average 39 ± 25 (1 sigma) ppm H_2O (reported in Table 3.1). Lanzarote peridotites are modally dominated by olivine and orthopyroxene, with ≤5% clinopyroxene. As a result, mass balance calculations indicate that the bulk water is controlled by the orthopyroxene water concentrations and abundance. Spinel Cr#, used as a proxy for melt depletion, is plotted against pyroxene water contents showing an overall correlation with higher water concentration in less melt depleted samples (lower Cr#; Figure 4.13c-d).

Figure 4.1. Representative peridotite xenolith in host basalt (LBLZ23-007).

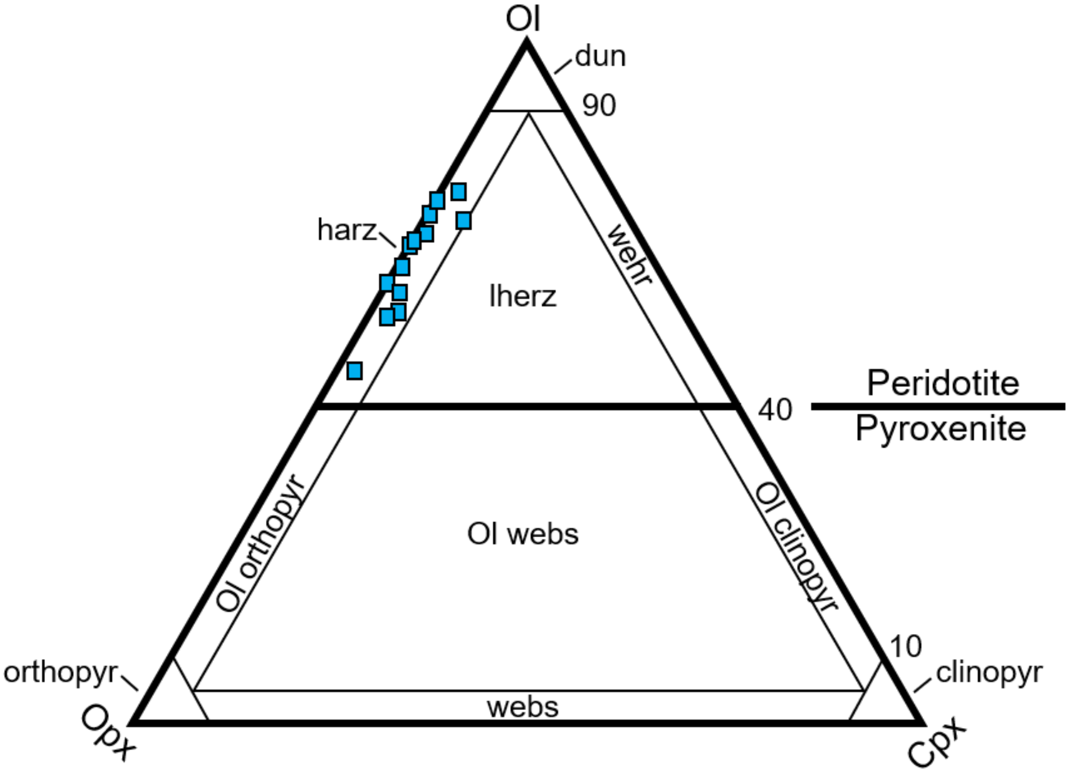

Figure 4.2. Ternary plot of Lanzarote peridotite mineralogy (this study). Abbreviations: Cpx = clinopyroxene, clinopyr = clinopyroxenite, dun = dunite, harz = harzburgite, lherz = lherzolite, Ol = olivine, Opx = orthopyroxene, othopyr = orthopyroxenite, webs = websterite, wehr = wehrlite.

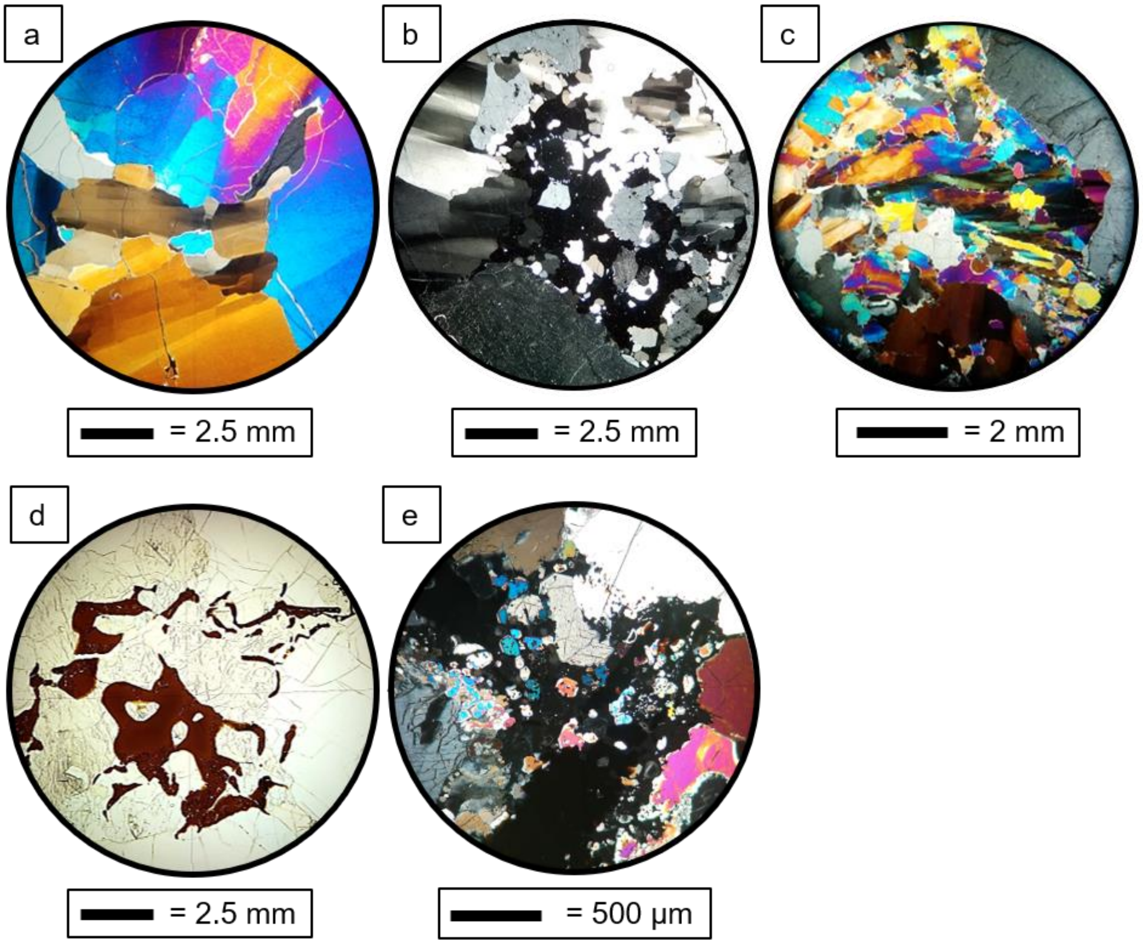

Figure 4.3. Microphotographs of representative textures of Lanzarote peridotites. Microphotographs 4.3(a – c, e) are shown in cross polarized light and (d) in plane polarized light. Textures shown represent protogranular olivine with kink bands (4.3a, LBLZ23-006), porphyroclastic textured grains (4.3b, LBLZ23-007), strained olivine (4.3c, LBLZ23-010), sponge spinel (4.3d, LBLZ23-012), and spinel pyroxene cluster + melt inclusions at its protogranular grain boundary (4.3e, LBLZ36-004).

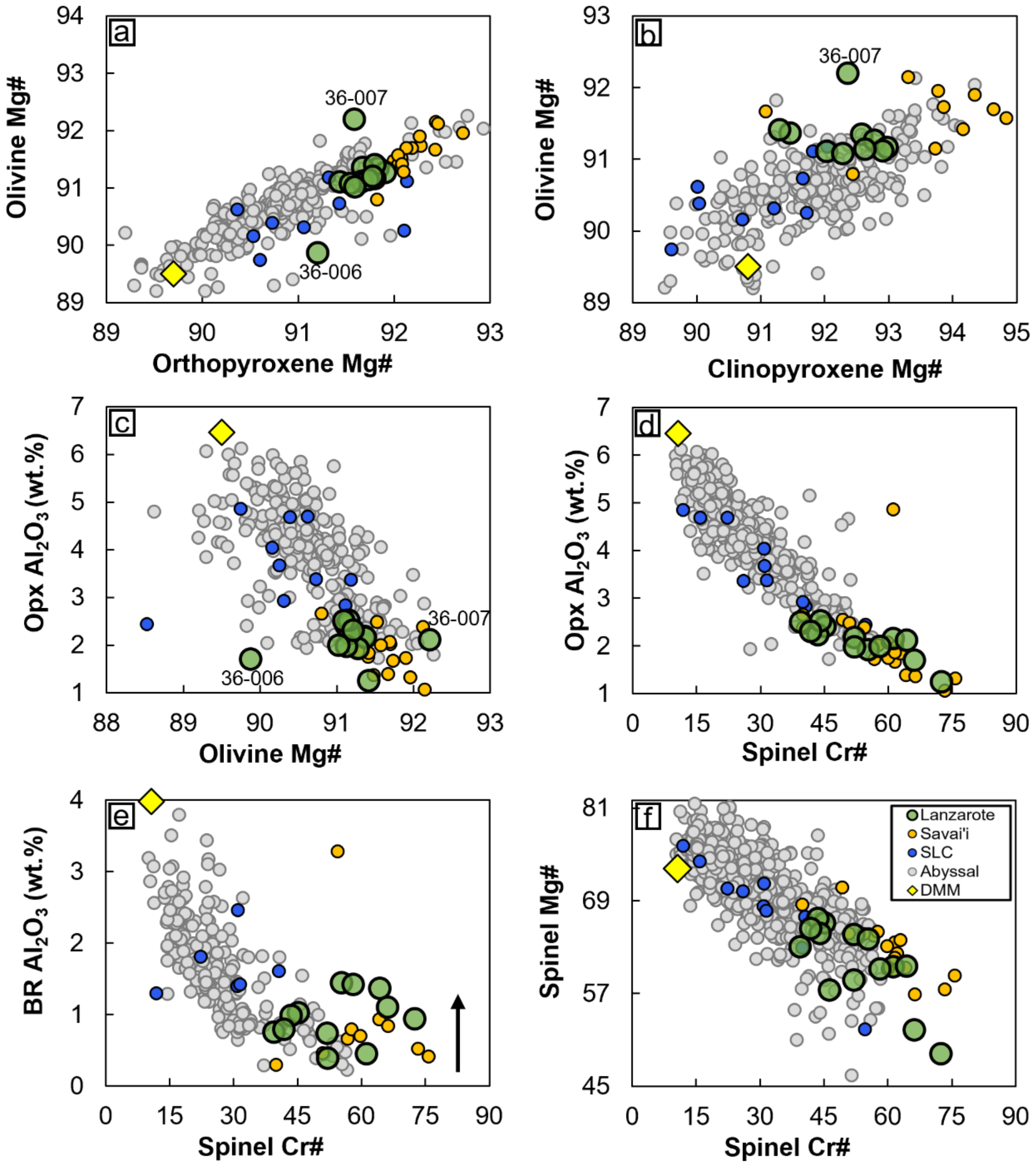

Figure 4.4. Major element plots of Lanzarote, Abyssal Peridotites, Salt Lake Crater (SLC), and Savai'i Samoa (SLC, Abyssal, Savai'i; Bizimis and Peslier, 2015, Warren 2016, Ashley et al., 2020; respectively). Depleted mantle contents plotted from Workman and Hart (2005) for comparison.

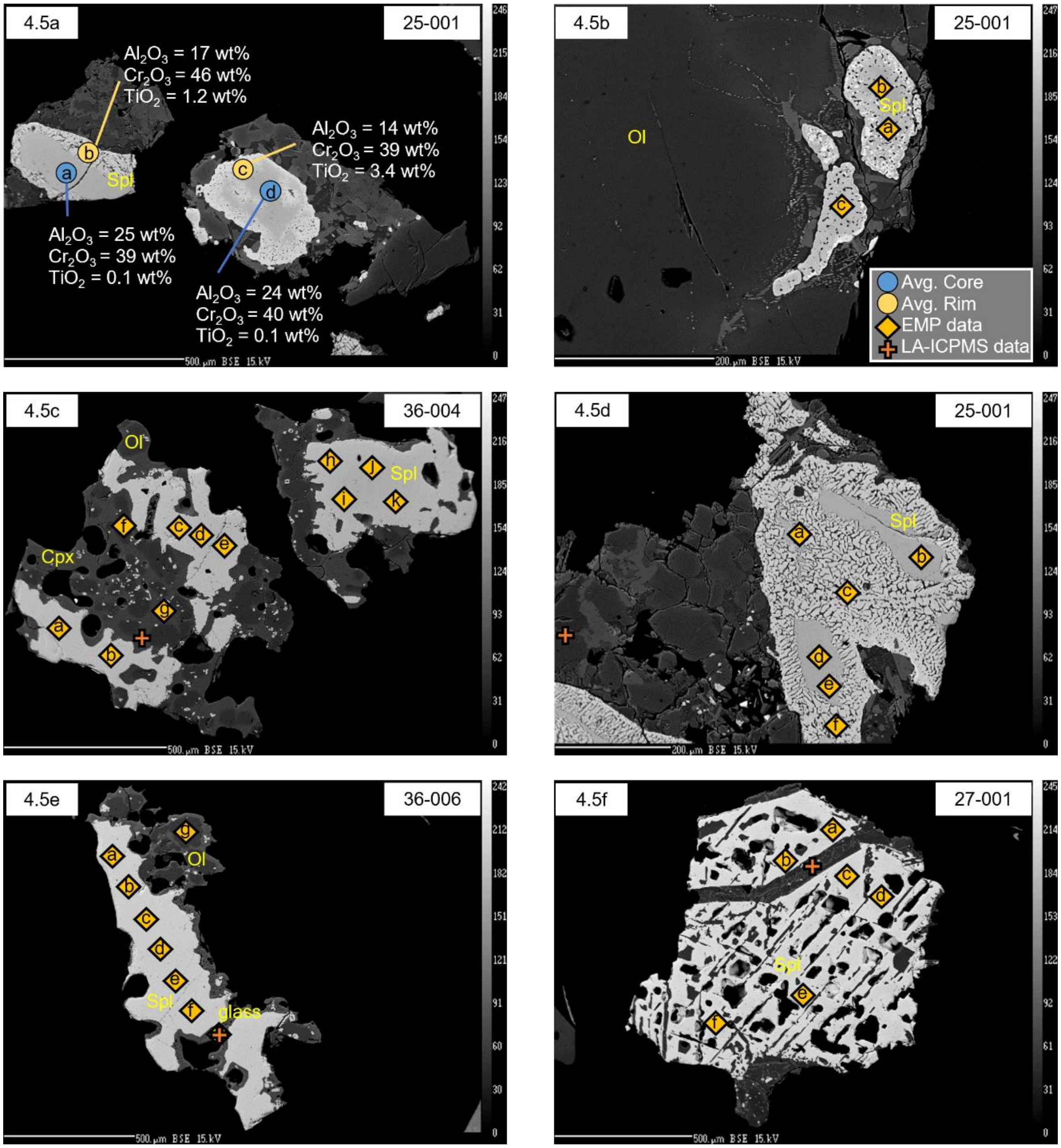

Figure 4.5. BSE of spinels from Lanzarote peridotites. 4.4a shows zoned spinels with averaged Cr_2O_3, Al_2O_3, and TiO_2 concentrations at core and rim of two spinel grains. 4.4b-f shows the textural complexity of spinel grains. Microphotographs captured with NASA Johnson Space Center Electron Microprobe. See Table 4.1 for all associated major and trace element data (Abbreviation(s): Avg. = average, Ol = olivine, Cpx = clinopyroxene Spl = spinel).

Table 4.1. Major and trace element data associated with Figure 4.5 spinels

	25-001 Fig. 4.5a (a)	25-001 Fig. 4.5a (b)	25-001 Fig. 4.5a (c)	25-001 Fig. 4.5a (d)
SiO_2	0.03	0.05	0.09	0.02
TiO_2	0.09	1.15	3.43	0.05
Al_2O_3	25.41	17.18	13.66	24.33
Cr_2O_3	39.43	45.94	39.14	40.50
FeO	20.41	22.38	33.18	21.09
MnO	0.23	0.28	0.37	0.21
MgO	14.85	13.16	9.22	14.08
NiO	0.20	0.08	0.17	0.17
CaO	0.00	0.03	0.10	0.01
Na_2O				
Total	100.6	100.3	99.3	100.4
Spl Cr#	46	55	46	48

	25-001 Fig. 4.5b (a)	25-001 Fig. 4.5b (b)	25-001 Fig. 4.5b (c)	25-001 Fig. 4.5b (Ol)
SiO_2	0.02	0.00	0.04	40.53
TiO_2	0.28	0.18	1.52	0.01
Al_2O_3	20.85	20.82	13.56	0.01
Cr_2O_3	42.68	42.35	48.36	0.01
FeO	17.44	17.93	17.05	9.30
MnO	0.49	0.44	0.46	0.14
MgO	17.99	17.53	18.00	49.80
NiO	0.15	0.23	0.07	0.38
CaO	0.04	0.00	0.17	0.06
Na_2O				0.01
Total	99.9	99.5	99.2	100.3
Spl Cr#	45	46	52	

	36-004 Fig. 4.5c (a)	36-004 Fig. 4.5c (b)	36-004 Fig. 4.5c (c)	36-004 Fig. 4.5c (d)
SiO_2	0.00	0.02	0.00	0.00
TiO_2	0.05	0.05	0.07	0.06
Al_2O_3	19.48	19.37	20.09	21.05
Cr_2O_3	46.52	46.47	45.33	44.49
FeO	17.73	17.99	18.36	19.06
MnO	0.18	0.17	0.26	0.18
MgO	15.58	15.58	15.29	15.22
NiO	0.11	0.19	0.22	0.18
CaO	0.02	0.01	0.02	0.01
Na_2O				
Total	99.7	99.8	99.6	100.3
Spl Cr#	55	54	53	52

	36-004 Fig. 4.5c (e)	36-004 Fig. 4.5c (f) Ol	36-004 Fig. 4.5c (g)	36-004 Fig. 4.5c (h)
SiO_2	0.00	40.62	60.49	0.02
TiO_2	0.06	0.00	0.17	0.04
Al_2O_3	21.01	0.06	17.55	19.74
Cr_2O_3	44.75	0.17	0.07	47.11
FeO	18.02	7.68	3.48	17.97
MnO	0.21	0.13	0.07	0.19
MgO	15.87	50.89	4.00	15.72
NiO	0.13	0.30	0.00	0.17
CaO	0.01	0.20	8.13	0.00
Na_2O		0.01	4.35	
Total	100.1	100.1	98.3	101.0
Spl Cr#	52			55

	36-004 Fig. 4.5c (i)	36-004 Fig. 4.5c (j)	36-004 Fig. 4.5c (k)	25-001 Fig. 4.5d (a)
SiO_2	0.04	0.03	0.01	0.04
TiO_2	0.04	0.05	0.03	0.08
Al_2O_3	22.36	21.96	24.06	25.62
Cr_2O_3	43.00	43.55	40.54	39.11
FeO	19.88	19.38	20.06	20.64
MnO	0.21	0.23	0.20	0.17
MgO	14.97	15.22	15.05	14.66
NiO	0.19	0.16	0.23	0.20
CaO	0.02	0.02	0.02	0.02
Na_2O				
Total	100.7	100.6	100.2	100.5
Spl Cr#	50	50	47	45

	25-001 Fig. 4.5d (b)	25-001 Fig. 4.5d (c)	25-001 Fig. 4.5d (d)	25-001 Fig. 4.5d (e)
SiO_2	0.03	0.02	0.04	0.04
TiO_2	0.10	0.56	0.09	0.08
Al_2O_3	25.39	15.39	25.39	24.57
Cr_2O_3	40.14	50.56	39.40	39.53
FeO	20.05	20.47	20.20	20.00
MnO	0.12	0.34	0.23	0.16
MgO	15.10	12.59	14.77	15.02
NiO	0.17	0.10	0.23	0.18
CaO	0.01	0.03	0.00	0.03
Na_2O				
Total	101.1	100.1	100.3	99.6
Spl Cr#	46	65	46	46

	25-001 Fig. 4.5d (f)	36-006 Fig. 4.5e (a)	36-006 Fig. 4.5e (b)	36-006 Fig. 4.5e (c)
SiO_2	0.02	0.03	0.06	0.02
TiO_2	0.49	0.68	0.72	0.74
Al_2O_3	15.05	15.93	15.68	15.92
Cr_2O_3	51.33	47.41	47.82	47.53
FeO	19.67	22.50	22.92	23.40
MnO	0.30	0.28	0.29	0.33
MgO	13.07	13.01	13.24	12.80
NiO	0.07	0.15	0.14	0.15
CaO	0.02	0.01	0.01	0.01
Na_2O				
Total	100.0	100.0	100.9	100.9
Spl Cr#	65	57	57	57

	36-006 Fig. 4.5e (d)	36-006 Fig. 4.5e (e)	36-006 Fig. 4.5e (f)	36-006 Fig. 4.5e (g) Ol
SiO_2	0.03	0.02	0.02	39.93
TiO_2	0.74	0.70	0.71	0.02
Al_2O_3	15.77	15.68	15.69	0.05
Cr_2O_3	47.31	47.54	46.96	0.20
FeO	22.79	23.03	23.05	11.83
MnO	0.25	0.26	0.28	0.20
MgO	13.07	13.00	13.03	47.82
NiO	0.22	0.15	0.19	0.28
CaO	0.00	0.00	0.09	0.24
Na_2O				0.02
Total	100.2	100.4	100.0	100.6
Spl Cr#	57	57	56	

	36-006 Fig. 4.5e (h)	27-001 Fig. 4.5f (a)	27-001 Fig. 4.5f (b)	27-001 Fig. 4.5f (c)
SiO_2	50.83	0.00	0.02	0.01
TiO_2	2.17	0.02	0.01	0.05
Al_2O_3	13.79	10.11	10.48	15.38
Cr_2O_3	0.26	52.67	52.46	42.56
FeO	8.60	22.82	23.24	26.87
MnO	0.16	0.28	0.26	0.25
MgO	7.08	13.33	13.33	13.69
NiO	0.02	0.07	0.17	0.27
CaO	11.91	0.01	0.00	0.00
Na_2O	2.94			
Total	97.8	99.3	100.0	99.1
Spl Cr#		62	62	46

	27-001 Fig. 4.5f (d)	27-001 Fig. 4.5f (e)	27-001 Fig. 4.5f (f)
SiO_2	0.00	0.00	0.00
TiO_2	0.02	0.02	0.03
Al_2O_3	13.59	12.39	12.43
Cr_2O_3	46.25	48.33	48.43
FeO	26.07	25.26	24.43
MnO	0.24	0.27	0.25
MgO	13.52	13.49	13.66
NiO	0.19	0.25	0.18
CaO	0.01	0.00	0.03
Na_2O			
Total	99.9	100.0	99.4
Spl Cr#	51	55	55

	36-004 Fig. 4.5c	25-001 Fig. 4.5d	36-006 Fig. 4.5e	27-001 Fig. 4.5f
Sc	50.74	57.24	35.16	41.06
Ti	7611.43	757.04	16261.38	194.21
V	238.32	155.31	235.86	469.61
Cr	868.60	5810.21	1168.49	754.63
Ni	104.18	356.45	139.43	65.20
Rb	12.42	2.53	25.69	81.01
Sr	671.64	89.77	764.40	843.03
Y	22.03	2.96	20.33	20.75
Zr	402.70	16.08	311.25	56.90
Nb	153.35	0.28	105.95	236.72
Cs		0.67	0.23	1.24
Ba	178.99	7.61	339.10	808.43
La	19.68	3.31	36.26	24.20
Ce	68.94	11.40	86.63	74.69
Pr	10.21	1.33	10.82	9.75
Nd	46.79	5.02	46.26	40.33
Sm	10.53	1.06	8.92	8.40
Eu	3.34	0.41	3.20	2.77
Gd	7.62	1.32	6.84	6.05
Tb	1.13	0.14	1.02	0.92
Dy	5.30	0.64	4.80	4.65
Ho	0.85	0.11	0.81	0.79
Er	2.13	0.28	1.89	1.93
Tm	0.25	0.04	0.23	0.25
Yb	1.44	0.26	1.52	1.52
Lu	0.19	0.04	0.17	0.20
Hf	7.02	0.11	7.49	0.40
Ta	8.20	0.01	6.35	3.37
Pb	1.18	0.46	2.69	3.84
Th	0.45	0.09	2.45	1.34
U	0.13	0.03	0.75	0.44

Notes: Annotation for ‘Fig. 4.5x (x)’ refers to respective Figure 4.5 panel and associated microprobe spot ‘(x)’; sample prefix = ‘LBLZ-’.

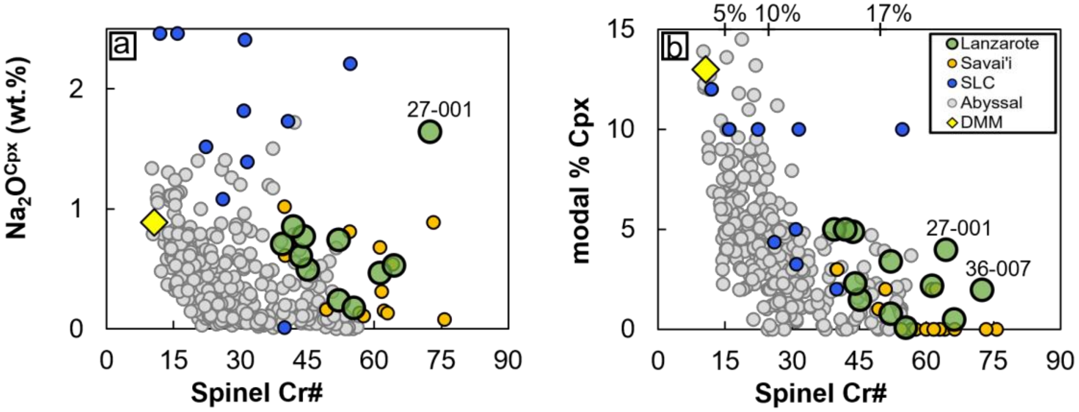

Figure 4.6. Na_2O^{Cpx} and Cpx modal abundance plotted against partial melting proxy, Spl Cr# of Lanzarote, Abyssal Peridotites, Salt Lake Crater (SLC), and Savai'i Samoa (SLC, Abyssal, Savai'i; Bizimis and Peslier, 2015, Warren 2016, Ashley et al., 2020; respectively). Depleted mantle contents plotted from Workman and Hart (2005) for comparison. 4.6(b) shows calculated 5%, 10% and 17% degrees of partial melting from spinel Cr# following methods in Hellebrand et al. (2001).

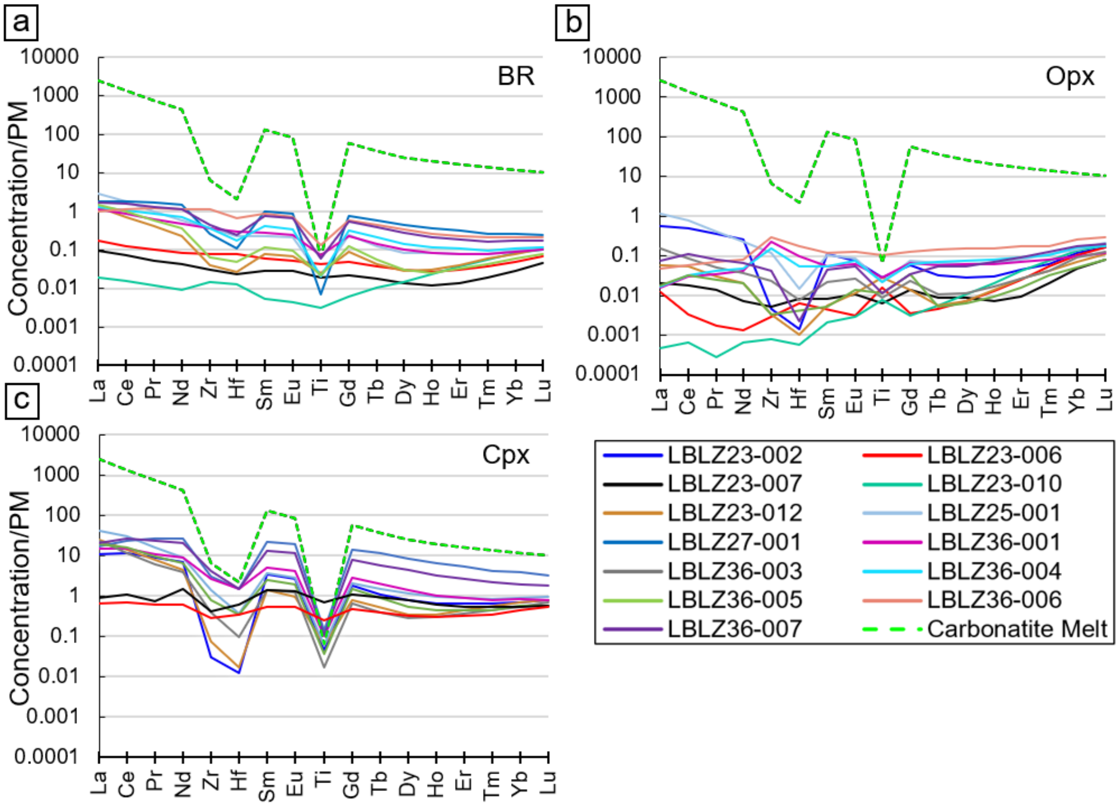

Figure 4.7. Lanzarote peridotites bulk rock (a), orthopyroxene (b), and clinopyroxene (c) trace element concentration normalized to the primitive mantle from McDonough and Sun (1995). Dashed green line is averaged carbonatite trace element concentrations from Fuerteventura, Canary Islands reported in Hoernle et al. (2001).

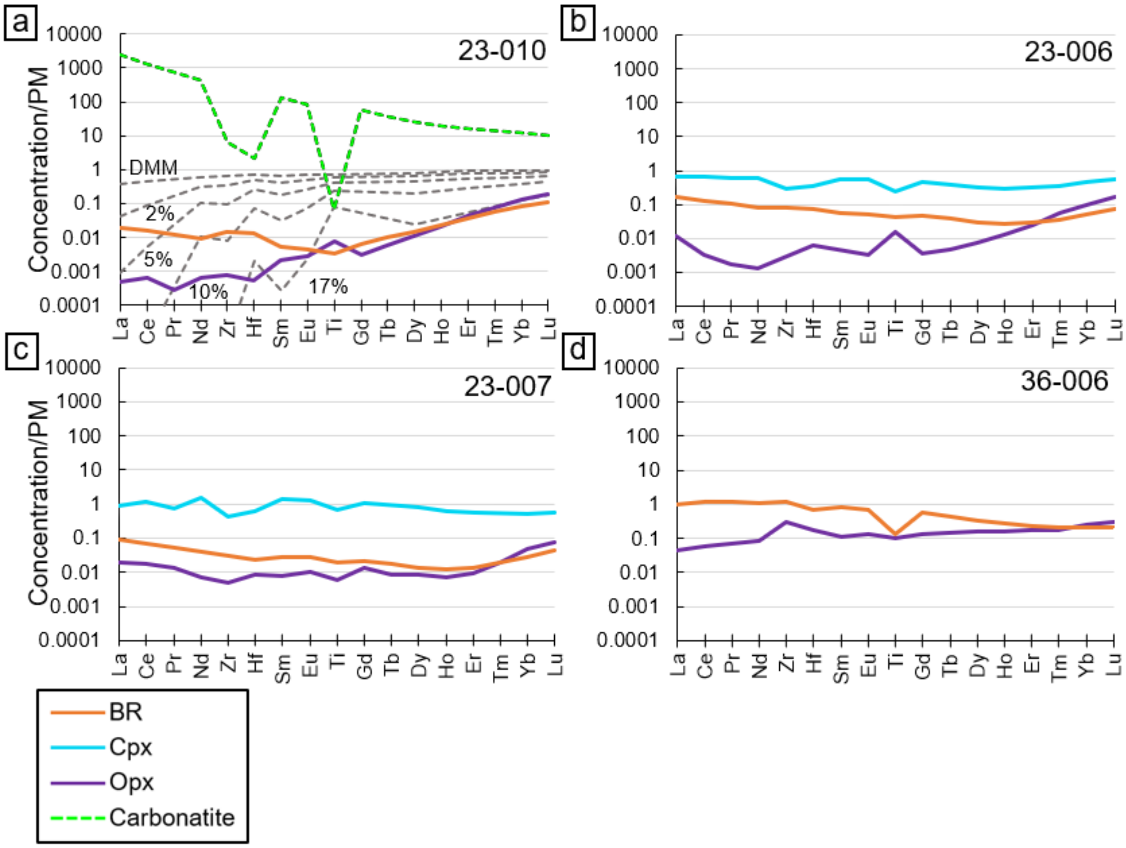

Figure 4.8. Group I peridotite trace element concentrations. Bulk rock, orthopyroxene, and when possible, clinopyroxene trace element concentrations are normalized to PM. Incremental batch melting model residues of a DMM source (Salters and Stracke 2003) at 0% 2%, 5%, 10%, and 17% partial melting are shown for comparison. Carbonatitic melt composition is plotted in 4.8a as a dashed green line. Sample prefix LBLZ for all samples, excluded in figure for simplicity.

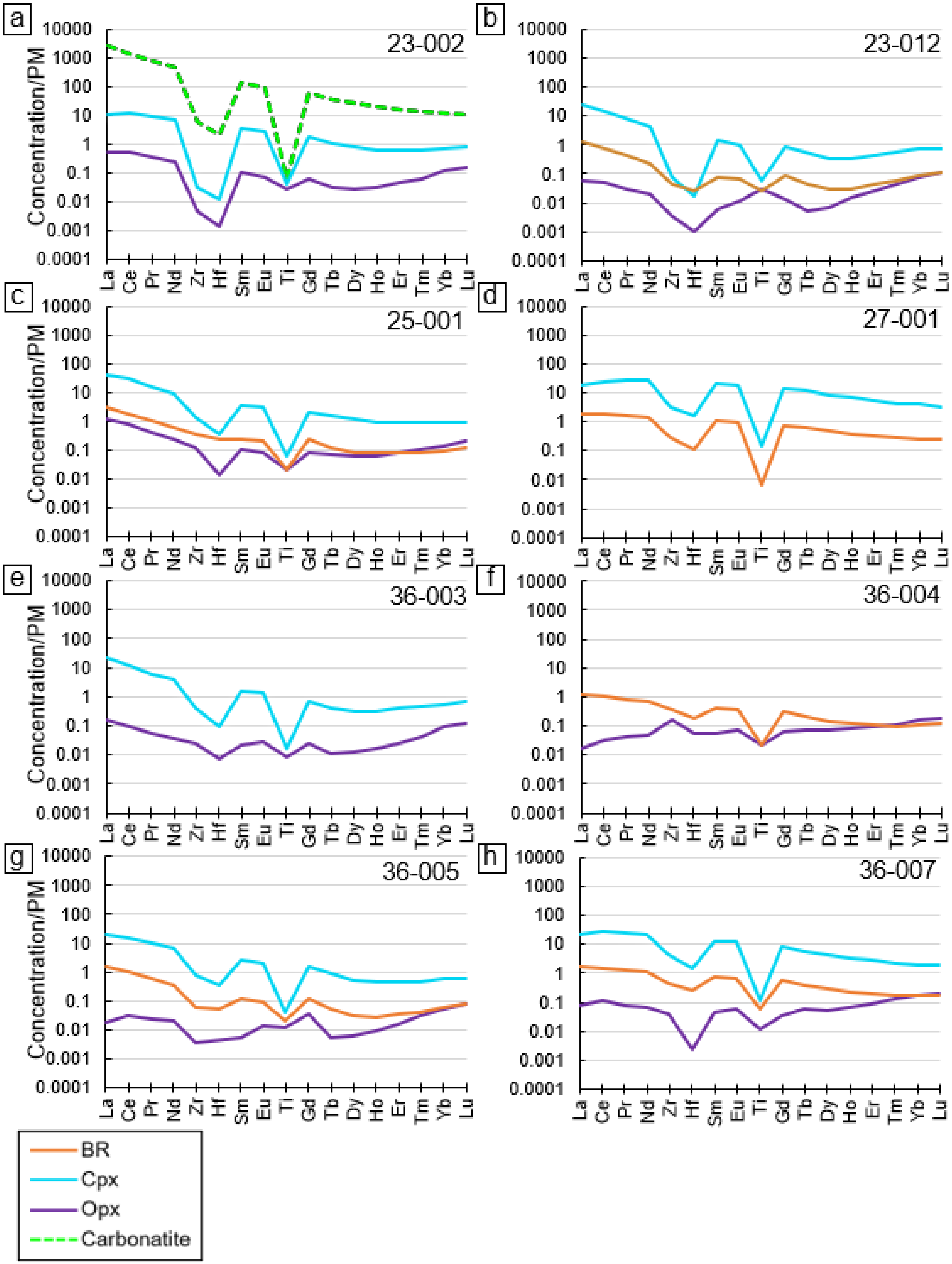

Figure 4.9. Group II peridotite trace element compositions. Shown are individual bulk rock, orthopyroxene and when possible clinopyroxene trace element concentrations, normalized to PM. Sample prefix LBLZ for all samples, excluded in figure for simplicity.

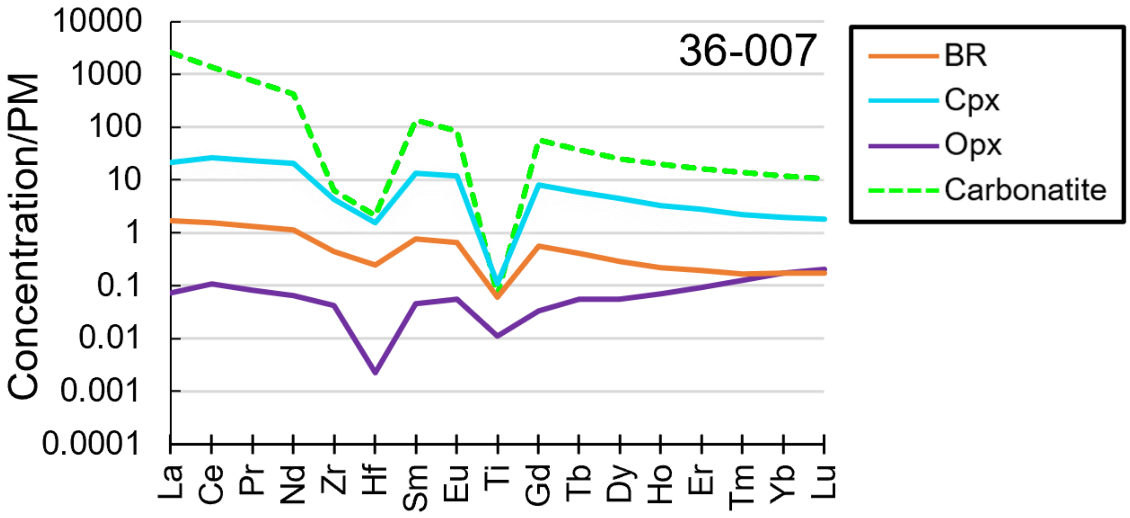

Figure 4.10. Group III peridotite trace element compositions. Bulk rock, orthopyroxene and clinopyroxene trace element concentrations shown, normalized to PM. Sample prefix LBLZ, excluded in figure for simplicity.

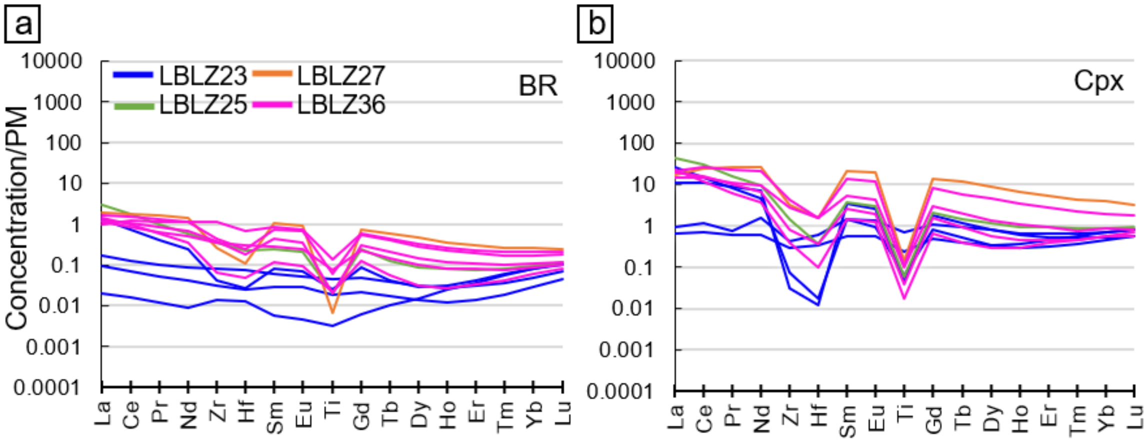

Figure 4.11. Trace element compositions by volcanic province normalized to PM from McDonough and Sun (1995). Provinces are Montana Colorada [LBLZ23], Salinas De Janubio [LBLZ25], Caldera de los Cuervos [LBLZ27], and El Cuchillo [LBLZ36]. Figure 8(a) shows bulk rock and (b) averaged clinopyroxene trace element compositions. Note the generally higher concentrations in the El Cuchillo samples.

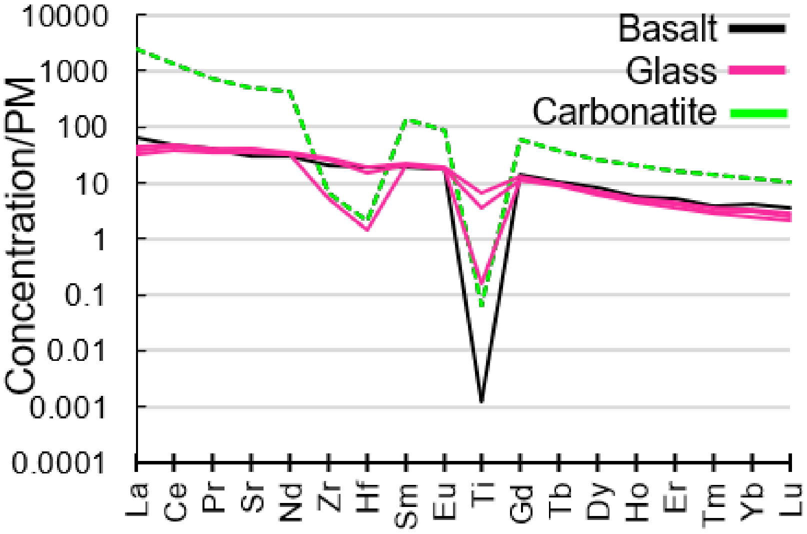

Figure 4.12. Trace element composition of glass inclusions. Carbonatite composition shown for comparison by dashed green line. Averaged trace element compositions from Lanzarote basalts shown for comparison by black line (basalt element concentrations from GEOROC: Ibarrola 1970; Brandle and Cerqueira, 1975; Sun and Hanson 1975; Sun 1980; Carracedo et al., 1990; Ovchinnikova et al., 1995; Hawkesworth et al., 1999; Widom et al., 1999; Neumann et al., 2000; Carracedo et al., 2003; Lundstrom et al., 2003; Aparicio et al., 2010; Geldmacher et al., 2011).

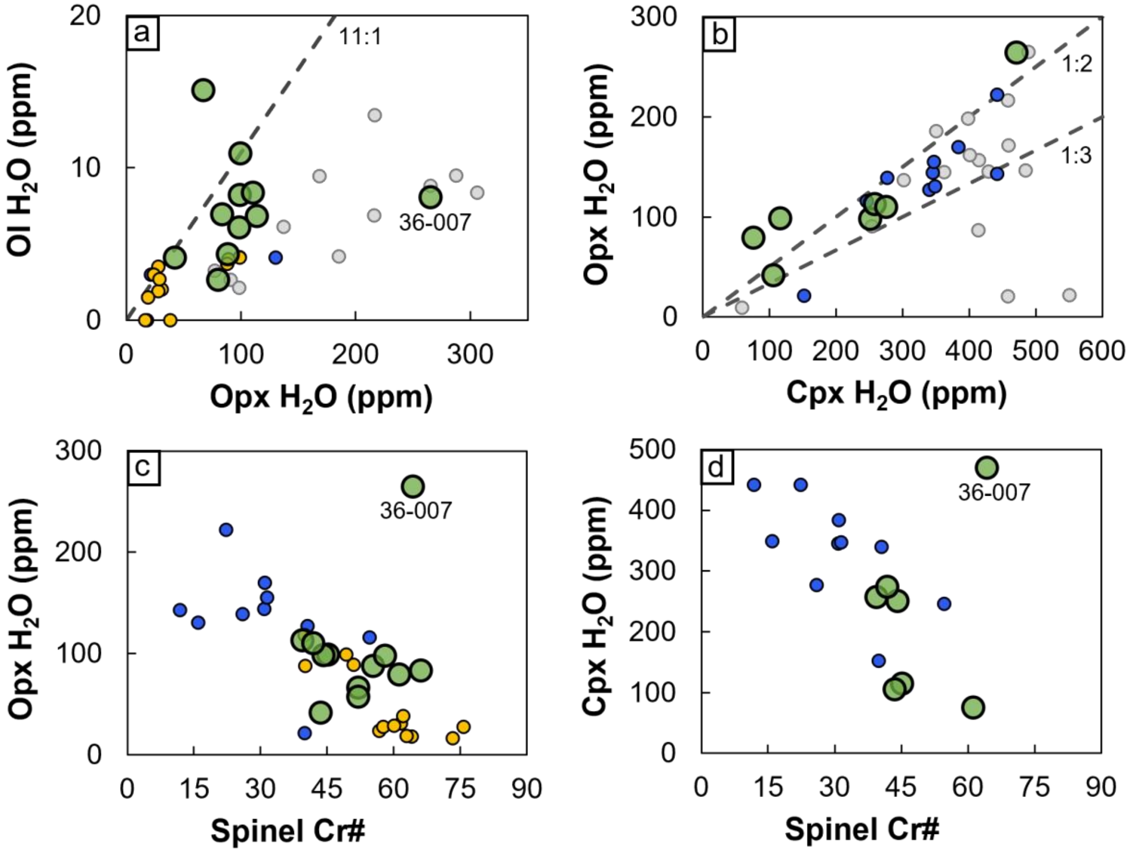

Figure 4.13. Water concentrations (shown as H_2O ppm) for Lanzarote peridotites. (a) olivine and orthopyroxene water concentrations; (b) orthopyroxene and clinopyroxene water concentrations. Dashed line represents the respective mineral partitioning of water content, discussed in the text. (c) and (d) represent melting degree (inferred from the spinel Cr#) compared to the pyroxene water concentrations. Water concentration and/or spinel Cr# datasets for SLC, Savai'i, and abyssal peridotites from Peslier et al. (2015), Ashley et al. (2020) and Warren and Hauri (2014); respectively.

CHAPTER 5

DISCUSSION

Here I discuss the contrasting effects of partial melting and melt infiltration on the water systematics of the lithospheric mantle beneath Lanzarote. The emerging view is that the peridotite water concentrations are not randomly distributed, but rather that metasomatism results in a systematic rehydration of the oceanic lithosphere.

5.1 Degree of melt depletion

Lanzarote peridotites record high degrees of melt depletion. Mineral and bulk rock major element compositions show high olivine Mg#, high spinel Cr# and low orthopyroxene Al_2O_3 contents overlapping with the most melt depleted oceanic peridotites (Figure 4.4). Orthopyroxene Al_2O_3 concentrations decrease with increasing spinel Cr#, consistent with melt extraction from the upper mantle (e.g., Jaques and Green, 1980) and are typically at equilibrium on the mineral scale. Lanzarote peridotites have undergone 15 to 22% melt depletion inferred from their bulk rock Al_2O_3 (following batch melting calculations and Al partitioning parameterization at 1 GPa detailed in Canil et al., 2002). Melt depletion estimates from spinel Cr# (using the parameterization of Hellebrand et al., 2001, and spinel grains with the lowest TiO_2 contents) indicate 15 to 21% partial melting, in agreement with the bulk rock Al_2O_3 estimates (see Table 3.3). These estimates overlap with those of other Lanzarote harzburgites from previous works (e.g., Siena et al., 1991, (F=10-20%); Neumann et al., 2004, [F=18-25%]). The significant overlap of the Lanzarote peridotite bulk rock and mineral major element compositions with those of abyssal peridotites, excluding Na_2O, is consistent with their origin as melt residues from the upper mantle.

5.2 Evidence for metasomatism

In contrast with the depletion, the Na_2O contents are enriched, particularly in the clinopyroxenes, indicating that Na is disturbed by other processes, like metasomatism (Figure 4.6a). The modal abundance of clinopyroxene is also higher than expected for samples that experienced such extensive partial melting, possibly suggesting the formation of secondary clinopyroxene due to melt addition (Figure 4.6b; e.g., sample LBLZ36-007). This may be explained by the reaction,

$$\text{Opx} + \text{carbonatite melt} \rightarrow \text{Cpx} + \text{Ol} + CO_2,$$

at pressures lower than 2 GPa (Wallace and Green 1988; Falloon and Green 1989). Additionally, the increases of Na_2O in clinopyroxene could be a result of a sodic carbonatite melt interaction with a peridotite (Yaxley et al., 1998).

All Lanzarote peridotites show enrichments in LREE, CaO in orthopyroxene (up to 1.4 wt. %), and Na_2O in clinopyroxene (up to 0.9 wt. %) relative to what is expected from the degree of melting. Light REE enrichments in peridotites, along with negative titanium anomalies (i.e., low Ti/Eu ratios), negative zirconium and hafnium anomalies and high Zr/Hf ratios are often attributed to carbonatitic metasomatism (e.g., Rudnick et al., 1993).

Increases in CaO and LREEs without enrichment in Al_2O_3 in orthopyroxene is also consistent with interaction with a carbonatitic magma which lacks Al (Dalton and Wood 1993; Dalton and Presnall 1998; Rudinick et al., 1993). At the same time, the increase of LREE, Ca, and Na has also been attributed to reaction with a silicate magma (Rivalenti et al., 2004; Perinelli et al., 2008), but it is unclear why this reaction does not also result in addition of Al, as in the case of the Lanzarote samples.

Na_2O vs. Nd (as a proxy for the LREE) can shed some additional light into the nature of metasomatism (Figure 5.1). Compared to other peridotites from the literature it is evident that the Lanzarote peridotites show a large increase in REE for little change in Nd. Instead, peridotites from Kilbourne Hole or Hawaii, show much higher Na for a given Nd. The two positive trends could be interpreted as silicate melt dominant metasomatism (shallow trend) and carbonatite metasomatism (steeper trend) for the Lanzarote, further supporting the arguments above based on the HFSE depletions relative to REE.

Melt-rock interaction is also evidenced in the petrographic observations and mineral compositions. Spinel-pyroxene composites and granoblastic pockets of olivine in association with clinopyroxene along grain boundaries, indicate secondary mineral assemblages either from trapped melts during melting of the primary lithology or as a product of melt -peridotite reaction / metasomatism (e.g., Bhanot et al., 2017, Dien et al., 2019).

Additionally, some peridotites have zoned spinel with core to rim element enrichments and depletions of Cr_2O_3 and Al_2O_3, respectively, that may be taken to imply melt depletion (e.g., high Spl Cr#; see Figure 4.5 and Table 4.1). The apparent enrichment of highly compatible Cr_2O_3 at the spinel rims may be an artifact from incompatible Al_2O_3 depletion from exchanges with a metasomatic melt (Patkó et al. 2020). In addition, most samples with zoned spinel also have higher concentrations of TiO_2 at their rims which is likely from interaction with a metasomatic melt (Dick and Bullen, 1984). LBLZ25-001 has complex spinel grains with adjacent silicate minerals mixed with feldspar. The association of olivine + plagioclase as crystals from melts results in Ti (an incompatible element in plagioclase and olivine) to become locally enriched in the residual melt and re-equilibrate with the adjacent spinel increasing its Ti contents (Rampone et al., 1991; Khedr and Arai, 2010). The removal of Al to the plagioclase also results in high Cr/Al in the residual melt possibly allowing for an explanation of the contrasting high Cr# and high Ti in the spinels as product of melt interaction.

5.2.1 Nature of metasomatism from trace element systematics

The trace element systematics of Lanzarote peridotites offer additional insights into melt depletion and metasomatic processes. All Lanzarote peridotite bulk rock and pyroxene LREE are enriched compared to their melt depletion estimates (Figures 4.8-4.10). Even the most REE depleted sample has REE enrichment compared to what is expected for pure melt extraction (LBLZ23-010, F = 18 to 21%; $(La/Yb)^{BR}_{PM} = 0.24$; Figure 4.8a). These trace element patterns cannot be explained simply by melting and instead imply LREE addition from metasomatism.

Group I peridotites have relatively flat REE profiles and are enriched for their estimated melting degree (e.g., LBLZ23-007, $(La/Yb)^{Cpx}_{PM} = 1.5$). These samples lack the negative Ti or Hf anomalies and thus likely equilibrated with a silicate melt. In contrast, Group II peridotites have bulk rock and pyroxene LREE enrichments and negative Zr, Hf, Ti anomalies, similar to trace element patterns of carbonatite magmas (Figure 4.7d; e.g., Rudnick et al., 1993; Klemme et al., 1995; Yaxley et al., 1998; Jones et al., 2013a). LBLZ36-001, classified as Group III, has bulk rock and orthopyroxene trace element concentrations without the strong negative Ti, Zr, Hf anomalies which are instead observed in its clinopyroxene. This suggests that Group III clinopyroxene trace elements may have (1) re-equilibrated with a carbonatite melt while the bulk rock and orthopyroxene trace elements reflect an older event of silicate metasomatism, or (2) the clinopyroxenes are the product of an infiltrating carbonatite melt and are secondary but without re-equilibration with the rest of the rock. In either case, this carbonatite melt interaction must have been transient and short-lived in duration in order to avoid equilibration with the bulk rock and orthopyroxene.

To better constrain the nature of the metasomatic agent we calculate the trace element concentrations of a putative melt in equilibrium with measured clinopyroxene trace elements using both carbonatite- and silicate melt partition coefficients and measured clinopyroxene trace element contents (Figure 5.2; Table 5.1). Most calculated melts strongly resemble carbonatite regardless of which set of partition coefficients is used and additionally match one measured glass composition from LBLZ27-001. In contrast, LBLZ23-006 and -007 have calculated melt trace element patterns that imply influence of a silicate melt (i.e., lack of Zr, Hf, Ti anomalies, lower LREE/HREE ratios than carbonatite). Therefore, Lanzarote peridotites experienced high degrees of melt extraction and have also experienced later metasomatism by presumably carbonatite and/ or silicate melt infiltrations.

5.3 Volcanic province heterogeneities

The trace element concentrations of the Montana Colorada peridotites (LBLZ23-) show lower extent of metasomatism and are more variable than peridotites of El Cuchillo ([LBLZ36-]; Figure 4.11). The Montana Colorada peridotites overall show larger influence from a silicate melt. In contrast, El Cuchillo peridotites show strong negative Ti, Zr, Hf anomalies and on greater LREE enrichments, and show influence from a carbonatite melt. The variability of Montana Colorada and El Cuchillo peridotites implies metasomatic heterogeneity at <10 km lateral scale in the lithosphere.

In addition, there is a correlation between peridotite equilibrium temperatures to volcanic province. El Cuchillo peridotites have, on average, equilibrated temperatures ~100°C less than Montana Colorada peridotites, possibly an indication of lower temperature carbonatite metasomatism and consequently lower viscosities. Yet, equilibration temperature and type of metasomatism proxied by the ratio $\mathrm{Ti/Eu}^{\mathrm{Cpx}}$ (low Ti/Eu taken as a proxy for carbonatite metasomatism) show no correlation. Thus, the differing equilibration temperatures are likely attributed to the local thermal structure of the mantle lithosphere. The two localities, Salinas De Janubio (LBLZ25-) and Caldera de los Cuervos (LBLZ27-) are not discussed as the sites may be under sampled.

5.4 The contrasting effects of melt depletion and metasomatism on water systematics

The (reconstructed) bulk rock water concentrations reflect the modal abundance of pyroxenes, which have significantly higher water contents than olivine, (section 4.4). Furthermore, the relative abundance of orthopyroxene and clinopyroxene plays an important role in the bulk rock water contents as clinopyroxene has approximately two times more water than orthopyroxene. Therefore, while bulk rock water concentrations are indicative, they are subject to mineral modal reconstruction uncertainties, particularly for small samples. In the following, we opt to compare the water contents of the peridotite minerals when analyzing the water systematics rather than the calculated bulk water contents.

The fact that the apparent $D_{H2O}^{mineral/mineral}$ is similar to the literature suggest that the water contents are likely in equilibrium between minerals on the peridotite hand specimen scale, and therefore likely reflect the water concentrations of these samples while in the lithosphere (see section 4.4). As previously discussed in section 5.1, Lanzarote peridotites have experienced high levels of melt depletion. As hydrogen is a highly incompatible element in the peridotite mineralogy, it will preferentially partition into the melt. Therefore, with increasing melt depletion, water contents in NAMs will decrease. Yet the water concentrations in NAMs and bulk rock Lanzarote peridotites are higher than expected for a given extent of melting (Figure 5.3). Consistent with the inferences for metasomatism above from lithophile elements, we attribute the variability in the water systematics to be the result of metasomatism.

Despite the strong evidence of carbonatitic metasomatism and the high-water contents, these water concentrations are not higher than other samples from the literature, particularly the SLC peridotites. The SLC peridotites have been pervasively metasomatized by silicate melts while the presence of pyroxenites as melt cumulates at the same location reinforces the presence of abundant melt in the Hawaiian lithosphere (Bizimis and Peslier, 2015; Peslier et al., 2015).

How then does interaction of carbonatite melts, affect the water systematics of peridotites and thus the lithospheric mantle? As previously discussed, most Lanzarote peridotites have elevated LREE (i.e., high $(La/Yb)_{PM}$) and negative Ti anomalies (i.e., low $(Ti/Eu)_{PM}$ ratios) indicative of carbonatite metasomatism interaction (Figure 5.4a-b). Using $(Ti/Eu)_{PM}$ then as a proxy for carbonatite metasomatism, we can compare the water contents of the pyroxenes in these samples and other oceanic peridotites. There is a positive correlation between increasing titanium depletion and water concentrations in Lanzarote clinopyroxenes and thus is inferred to be a result of carbonatite metasomatism (Figure 5.4b). In contrast, Lanzarote peridotites with minimal Ti depletions and characteristics of silicate metasomatism (classified as Group I), have the lowest clinopyroxene water concentrations of the suite of samples. This implies greater addition of water in the lithosphere due to carbonatitic metasomatism. Note however that despite the evidence for carbonatite metasomatism, the Lanzarote peridotites do not have particularly higher water concentrations than the SLC peridotites which show more of a silicate melt signatures.

To further explore the nature of water addition, we calculate the concentration of water in a putative melt in equilibrium with measured clinopyroxenes. Partition coefficients were calculated following methods in Novella et al. (2014) ($D_{H2O}^{Cpx/melt}$; see Table 5.2 footnote). These estimates suggest that the Lanzarote clinopyroxenes last equilibrated with a melt of ~1 to 4 wt.% H_2O. These estimates however are much lower than estimates for water contents in a carbonatite (~ 10 wt.% e.g., Dixon et al., 2008). These data results in two contrasting observations: a) carbonatite metasomatism results in water addition in the lithosphere and b) the amount of water added is less that that expected from equilibration with carbonatite metasomatism.

An additional clue comes from comparison of the water systematics with Ce concentrations. The H_2O/Ce ratio is often used as proxy of mantle sources in erupted magmas (e.g., Dixon et al, 2002). We calculate the H_2O/Ce ratio of the putative melt in equilibrium with the clinopyroxene. These H_2O/Ce ratios are very low (<75) unlike any eruptive magmas from the oceanic mantle (>50) and unlike estimates for carbonatites (~ 250). Therefore, this implies either water loss from the xenoliths to the surface, or that the calculated putative melts are incorrect. Preliminary water transects across minerals show no significant loss of water. Moreover, one would expect that water loss would be a random process, therefore the H_2O/Ce ratios would not correlate with anything. Instead, they correlate with Ti/Eu, confirming that these are primary features (Figure 5.4). Therefore, water loss is unlikely to have resulted in the low H_2O/Ce.

The alternative is that the partition coefficients we used for calculating the water concentrations of the putative melt are not appropriate for clinopyroxene and carbonatite. Yang et al., (2015) and Guo et al., (2020) have shown that water solubility in olivine and orthopyroxene, respectively, decreases roughly by a factor of 2 in the presence of CO_2 compared to CO_2 absent conditions. This may be due to the reduced activity of water in the presence of CO_2 in the melt. If this notion of reduced water activity in the orthopyroxenes is extended to the clinopyroxenes, then the apparent partition coefficient for water in the presence of CO_2 would be at least half of what is used here, and the calculated H_2O/Ce in the equilibrium melt would be at least two times greater, bringing these putative melts closer to erupted melt H_2O/Ce ratios. Regardless of the mechanism the result is that while carbonatite metasomatism adds water in the lithosphere, it adds to a much lower extent than REE, resulting in rocks with very low H_2O/Ce ratios. This plume metasomatized lithosphere, upon recycling into the mantle, can generate enriched and low H_2O/Ce ratio domains that upon melting could generate magmas with low H_2O/Ce (Figure 5.5). The end result is that carbonatitic metasomatism results in both wet (increase water) and dry (low H_2O/Ce) metasomatized domains and may therefore provide an alternative explanation for the origin of low H_2O/Ce domains as recycled metasomatized lithosphere (e.g., Bizimis and Peslier, 2015) rather than dehydrated recycled lithosphere (Dixon et al. 2002).

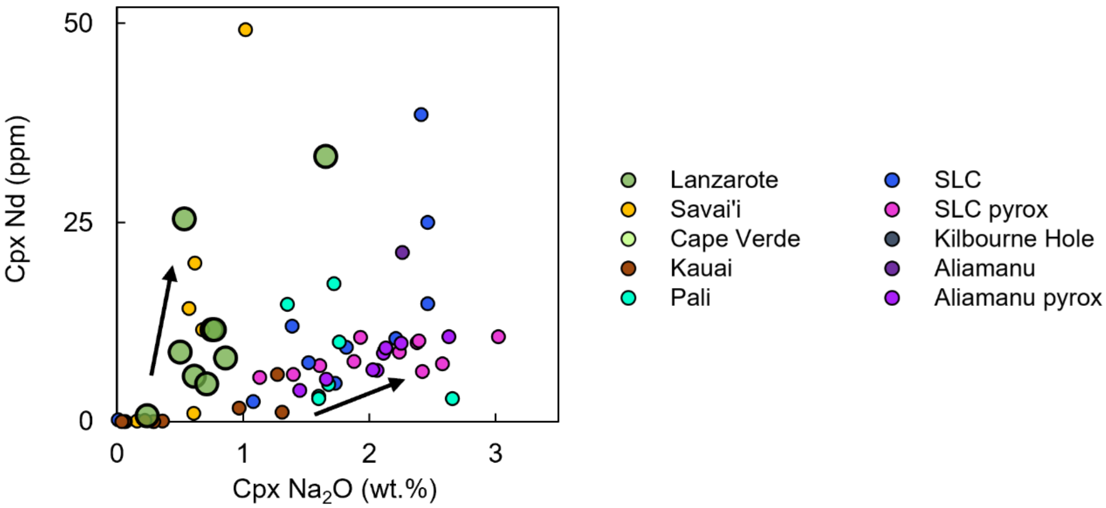

Figure 5.1. Na_2O vs. Nd of clinopyroxenes in oceanic peridotites. The arrow associated with the shallower trend indicates silicate melt dominant metasomatism and the arrow for the steeper trend, carbonatite metasomatism. Data from Bell and Rossman (1992), Grant et al. (2007), Bonadimen et al. (2009), Harvey et al. (2012), Warren and Hauri (2014), Bizimis and Peslier (2015), Peslier and Bizimis (2015), Peslier et al. (2015), Schaffer et al. (2019), Ashley et al. (2020), Bizimis et al. *unpublished*, and this study.

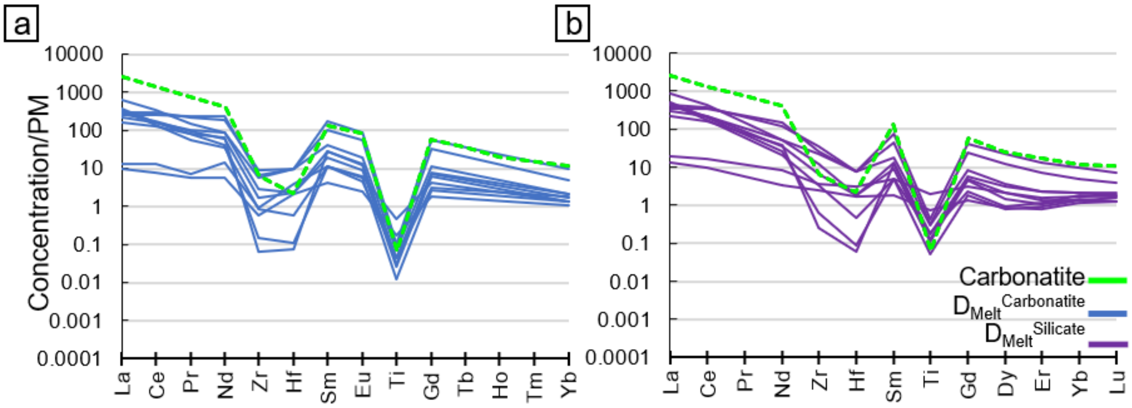

Figure 5.2. Calculated D_{melt}^{Cpx} trace elemental concentrations normalized to PM. Melts calculated by measured clinopyroxenes in equilibrium with (a) carbonatite and (b) silicate melt. Partition coefficients used are shown in Table 5.1. Carbonatite composition is plotted for comparison.

Table 5.1. Carbonatite- and silicate melt partition coefficients used to calculate the trace element concentrations of a putative melt in equilibrium with measured clinopyroxene trace elements in associated Figure 5.2.

	Cpx/carb. melt[1]	Cpx/sil. melt[2]
Ti	1.42	0.34
V	2.93	
Sr	0.08	0.095
Y	0.3	0.412
Zr	0.48	0.119
Nb	0.1	0.004
Ba	0.07	
La	0.07	0.049
Ce	0.09	0.07
Pr	0.11	
Nd	0.11	0.178
Sm	0.13	0.293
Eu	0.22	
Gd	0.26	0.35
Dy	0.29	0.38
Er	0.41	0.4
Yb	0.41	0.4
Lu	0.41	0.449
Hf	0.16	0.2
Ta	0.15	

Notes: (1) = $D_{\text{carbonatite melt}}^{element}$ from Klemme et al. (1995); (2) = $D_{\text{silicate melt}}^{element}$ from Johnson (1998). Abbreviations: carb. = carbonatite; sil. = silicate.

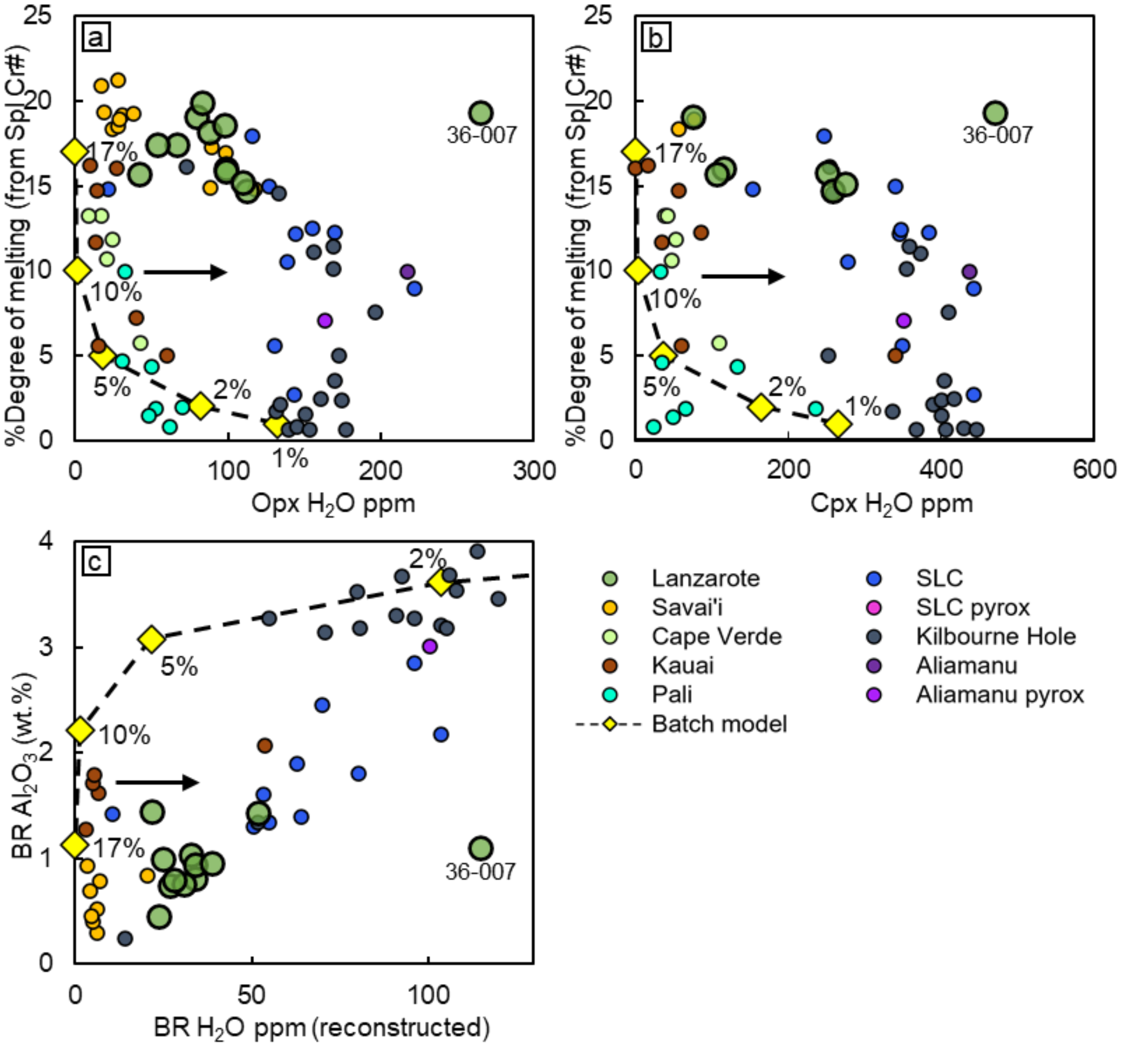

Figure 5.3. Water concentrations plotted with degree of melting. Incremental batch melting model residues of a DMM source (Salters and Stracke 2003) are shown for comparison with initial bulk rock water concentration at 270 ppm and at 1% porosity assumed for 1%, 2%, 5%, 10%, and 17% partial melting are shown for comparison. Arrows point to the shift in higher water contents for a given amount of melt depletion and thus attributed to metasomatism. Oceanic peridotite data from Bell and Rossman (1992), Grant et al. (2007), Bonadimen et al. (2009), Harvey et al. (2012), Warren and Hauri (2014), Bizimis and Peslier (2015), Peslier and Bizimis (2015), Peslier et al. (2015), Schaffer et al. (2019), Ashley et al. (2020), Bizimis et al. *unpublished*, and this study.

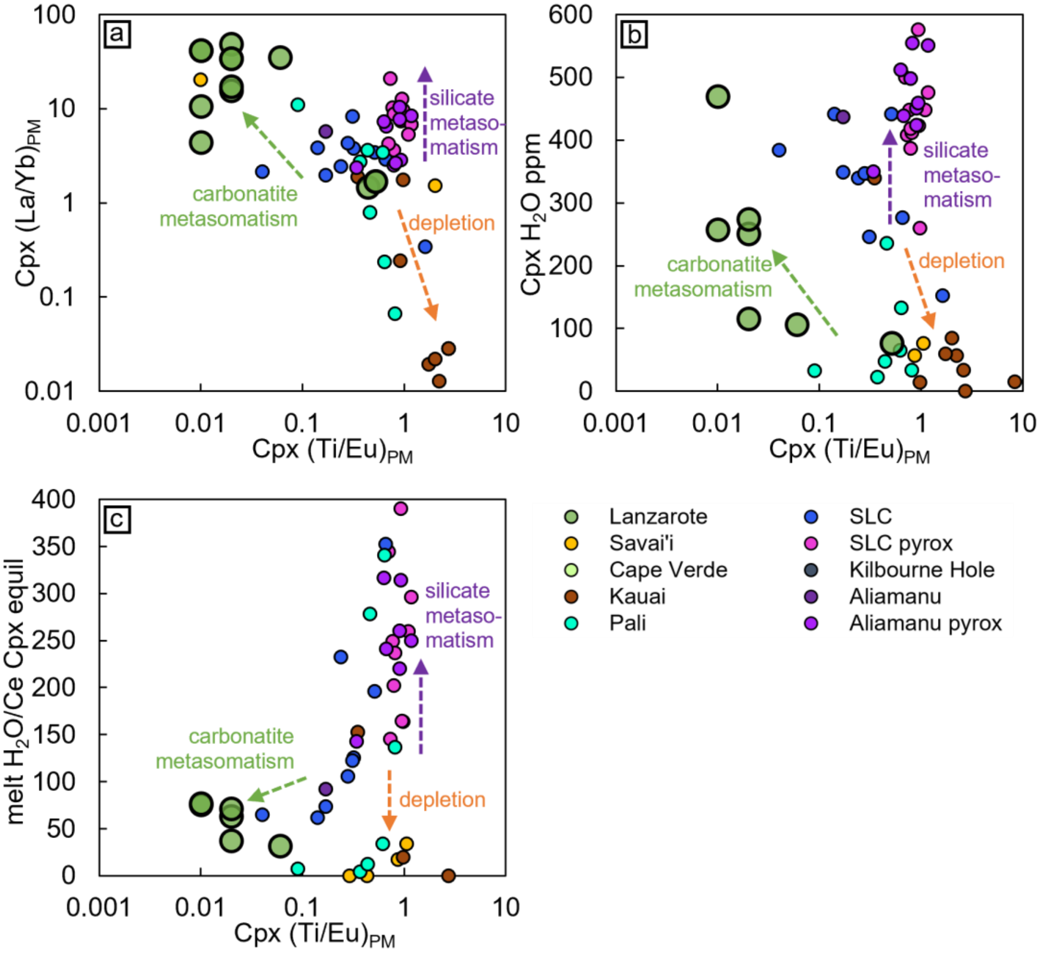

Figure 5.4. REE concentrations and water distributions of oceanic peridotites. Clinopyroxene Ti/Eu ratios normalized to primitive mantle (from McDonough and Sun, 1995). Arrows indicate type of metasomatism deviation trends (carbonatite vs. silicate). Oceanic peridotite data from Bell and Rossman (1992), Grant et al. (2007), Bonadimen et al. (2009), Harvey et al. (2012), Warren and Hauri (2014), Bizimis and Peslier (2015), Peslier and Bizimis (2015), Peslier et al. (2015), Schaffer et al. (2019), Ashley et al. (2020), Bizimis et al. *unpublished*, and this study.

Table 5.2. Water partition coefficients in equilibrium with clinopyroxene and melt.

Sample	$D_{H2O}^{cpx/melt\ (1)}$
LBLZ23-002	0.012
LBLZ23-006	0.012
LBLZ23-007	0.008
LBLZ23-010	0.008
LBLZ23-012	0.011
LBLZ25-001	0.011
LBLZ27-001	0.013
LBLZ36-001	0.012
LBLZ36-003	0.012
LBLZ36-004	0.008
LBLZ36-005	0.012
LBLZ36-006	0.008
LBLZ36-007	0.011

Note: (^{1}) = calculations following [$D_{H2O}^{cpx/melt} = 0.0016 * Al_2O_3$(wt.%) + 0.0078] from Novella et al. (2014).

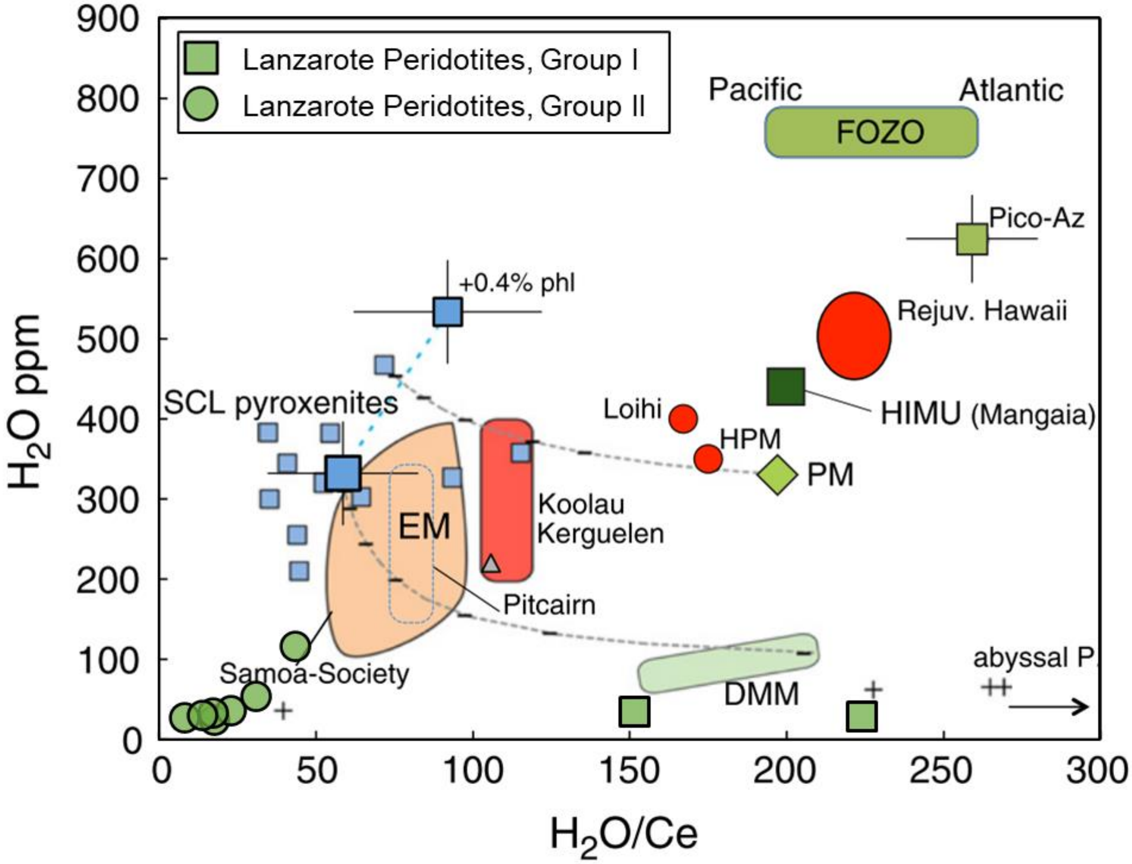

Figure 5.5. H_2O/Ce ratios and bulk water contents for Lanzarote peridotites. Group I Lanzarote peridotites last equilibrated with a silicate melt shown by their trace element concentrations and Group II with a carbonatite melt (see Section 5.2.1). Figure modified from Bizimis and Peslier (2015).

CHAPTER 6

CONCLUSIONS AND SIGNIFICANCE

Peridotite xenoliths from Lanzarote island in the Canaries represent fragments of the east Atlantic lithosphere that has interacted with melts from the Canaries plume. The analyzed peridotites have experienced high degrees of melting evidenced by their major element concentrations and petrographic observations and overlap with some of the most refractory oceanic peridotites. Yet, their trace elemental systematics show LREE enrichments relative to HREE, inconsistent for their extensive melting estimates. Thus, their bulk rock and pyroxene element concentrations show re-equilibration with infiltrating melts. The majority of Lanzarote peridotites show Zr, Hf, and Ti depletions relative to the adjacent REE in a mantle incompatibility diagram, indicating equilibration with carbonatite melts. Few samples without these depletions show interaction with silicate melt. The peridotites from volcanic province of El Cuchillo and Montana Colorada have distinct trace element systematics suggesting heterogenous lithosphere and plume lithosphere interaction at <10km scale.

The Lanzarote peridotite water contents are higher for what melting models predict, but still lower than estimates of the Depleted upper mantle. The samples with strong evidence of carbonatite metasomatism have higher water concentrations. Therefore, carbonatitic metasomatism in the oceanic lithosphere results in increase in water concentrations. Yet, recalculated melt water concentrations of putative melts in equilibrium with Lanzarote clinopyroxenes (~1 to 4 wt.%) are much lower than that of carbonatites (~ 10 wt.%). Importantly, the low calculated H_2O/Ce ratios (<75) of those putative melts correlate with carbonatite metasomatism proxies suggesting that the observed water contents (and therefore the inferred melt water contents) are a primary feature rather than simply an effect of diffusive loss of hydrogen upon xenolith ascent to the surface. A possible explanation for the low H_2O/Ce observed in the peridotites and the calculated putative melts is that the water partition coefficients between clinopyroxene and a melt are different between silicate and carbonatite melt, and in particular the clinopyroxene / carbonatite water partition coefficients may be at least 2 times lower than that of clinopyroxene / silicate. Therefore, carbonatite metasomatism results in high water contents but low water/Ce ratios creating an apparent contrast between "wet" (high water) and "dry" (low H_2O/Ce) geochemical characteristics. Low H_2O/Ce ratios in erupted mantle magmas were previously attributed to dehydrated recycled lithosphere in their source. Instead, this study provides an alternative explanation. Due to a lesser extent of water addition from carbonatitic metasomatism association than REE enrichments, the low H_2O/Ce ratios may therefore be from recycled metasomatized oceanic lithosphere such as observed in the Lanzarote plume metasomatized lithosphere.

REFERENCES

Aparicio A. Y., Tassinari C. C. G., Garcia R., Arana V. (2010). Sr And Nd Isotope Composition of The Metamorphic, Sedimentary And Ultramafic Xenoliths Of Lanzarote (Canary Islands): Implications for Magma Sources J. Volcanol. Geotherm. Res. 189, 143-150.

Ashley A.W., Bizimis M., Peslier A.H., Jackson K., (2020). Metasomatism and Hydration of the Oceanic Lithosphere: A Case Study of Peridotite Xenoliths from Samoa. Journal of Petrology, 770, egaa028.

Asimow, P. D., Dixon, J. E. & Langmuir, C. H. (2004). A hydrous melting and fractionation model for mid-ocean ridge basalts: Application to the Mid-Atlantic Ridge near the Azores. Geochemistry, Geophysics, Geosystems. John Wiley & Sons, Ltd 5, 1–24.

Banda, E., Danobeitia, J. J., Surinach, E., & Ansorge, J., (1981). Features of crustal structure under the Canary Islands. Earth Planet. Sci. Lett. 55, 11-24.

Bayon G., Barrat J.A., Etoubleau J., Benoit M., Bollinger C. and Révillon S. (2009). Determination of rare earth elements, Sc, Y, Zr, Ba, Hf and Th in geological samples by ICPMS after Tm addition and alkaline fusion. Geostandards and Geoanalytical Research, 33, 51–62.

Brandle J. L., Cerqueira M. I. (1975). Notes On Minor-Element Distribution In Basaltic Magmas Of The Old Series, Canary Islands. Estudios Geol. 31, 375-383.

Bell D. R. and Rossman G. R. (1992). Water in Earth's mantle: the role of nominally anhydrous minerals. Science 255, 1391–1397.

Bell, D. R., Ihinger, P. D. & Rossman, G. R. (1995). Quantitative analysis of trace OH in garnet and pyroxenes. American Mineralogist.

Bell, D. R., Rossman, G. R., Maldener, J., Endisch, D. & Rauch, F. (2003). Hydroxide in olivine: A quantitative determination of the absolute amount and calibration of the IR spectrum. Journal of Geophysical Research: Solid Earth. Wiley-Blackwell 108, 8–1 to 8–9.

Bhanot, K. K., Downes, H., Petrone, C. M., & Humphreys-Williams, E. (2017). Textures in spinel peridotite mantle xenoliths using micro-CT scanning: Examples from Canary Islands and France. Lithos, 276, 90–102.

Bizimis, M. & Peslier, A. H. (2015). Water in Hawaiian garnet pyroxenites: Implications for water heterogeneity in the mantle. Chemical Geology 397, 61–75.

Bonadiman C., Hao Y., Coltorti M., Dallai L., Faccini B., Huang Y., Xia Q.-K. (2009). Water contents of pyroxenes in intraplate lithospheric mantle. Eur. J. Mineral. 21, 637–647.

Brey, G. P., and Kohler, T., (1990). Geothermobarometry in Four-phase Lherzolites II. New Thermobarometers, and Practical Assessment of Existing Thermobarometers. Journal of Petrology 31, 1353-1378.

Canil, D. (2002). Vanadium in peridotites, mantle redox and tectonic environments: Archean to present. Earth Planet Sci Lett 195:75–90.

Carignan J., Hild P., Mevelle G., Morel J., Yeghicheyan D. (2001). Routine analyses of trace elements in geological samples using flow injection and low pressure on-line liquid chromatography coupled to ICP-MS: A study of geochemical reference materials BR, DR-N, UB-N, AN-G and GH. Geostandards Newsletter: The Journal of Geostandards and Geoanalysis, 25, 187–198.

Carracedo J. C., Rodriguez Badiola E., Soler V. (1990) Volcanic and Structural Aspects And Petrological Evolution of The Eruption Of 1730 on Lanzarote, Canary Islands Estudios Geol. 46, 25-55.

Carracedo, J.C., Day, S., Guillou, H., Rodríguez Badiola, E., Canas, J.A., Pérez Torrado, F.J., (1998). Hotspot volcanism close to a passive continental margin: the Canary Islands. Geological Magazine 135 (05), 591-604.

Carracedo J. C., Singer B. S., Jicha B. R., Guillou H., Rodriguez Badiola E., Meco J., Perez Torrado F. J., Gimeno D., Socorro S., Lainez A. (2003). The Eruption And The Volcanic Tube Of Corona Volcano (Lanzarote, Canary Islands) Estudios Geol. 59, 277-302.

Carracedo J.C., Perez-Torrado F.J., Rodriguez-Gonzalez A., Fernandez-Turiel J.L., Klugel A., Troll V.R., Wiesmaier S., (2012). "The ongoing volcanic eruption of El Hierro, Canary Islands. Eos American Geophysical Union, 93, 89-90.

Chauvel C., Bureau S. and Poggi C. (2011). Comprehensive chemical and isotopic analyses of basalt and sediment reference materials. Geostandards and Geoanalytical Research, 35, 125–143.

Chopra, P. N. & Paterson, M. S. (1984). The role of water in the deformation of dunite. Journal of Geophysical Research: Solid Earth. Wiley-Blackwell 89, 7861–7876.

Dalton, J. A., and Presnall, D. C., (1998), Carbonatitic melts along the solidus of model lherzolite in the system CaO- MgO-Al2O3-SiO2-CO2 from 3 to 7 GPa, Contrib. Mineral. Petrol., 131,123–135, doi:10.1007/s004100050383.

Dalton, J. A., and Wood, B. J., (1993) The composition of primary carbonate melts and their evolution through wall rock reactions in the mantle. Earth Planet Sci Lett 119: 511±525

Demouchy S., Tommasi A., Barou F., Mainprice D., and Cordier P., (2012). Deformation of olivine in torsion under hydrous conditions. Phys. Earth Planet. Inter. 202–203, 56–70.

Dick, H. J. B., & Bullen, T., (1984). Chromian spinel as a petrogenetic indicator in abyssal and alpine-type peridotites and spatially associated lavas. Contr. Miner. Petrol. 86, 54-76.

Dixon, J. E., Stolper, E. & Delaney, J. R. (1988). Infrared spectroscopic measurements of CO2 and H2O in Juan de Fuca Ridge basaltic glasses. Earth and Planetary Science Letters. Elsevier 90, 87–104.

Dixon, J. E. & Clague, D. A. (2001). Volatiles in Basaltic Glasses from Loihi Seamount, Hawaii: Evidence for a Relatively Dry Plume Component. Journal of Petrology. Oxford University Press 42, 627–654.

Dixon, J. E., Leist, L., Langmuir, C. & Schilling, J.-G. G. (2002). Recycled dehydrated lithosphere observed in plume-influenced mid-ocean-ridge basalt. Nature. Nature

Dixon, J. E., Clague, D. A., Cousens, B., Monsalve, M. L. & Uhl, J. (2008). Carbonatite and silicate melt metasomatism of the mantle surrounding the Hawaiian plume: Evidence from volatiles, trace elements, and radiogenic isotopes in rejuvenated-stage lavas from Niihau, Hawaii. Geochemistry, Geophysics, Geosystems. Wiley-Blackwell 9, 1–34. Publishing Group 420, 385–389.

Falloon, T.J., and Green, D.H. (1989) The solidus of carbonated, fertile peridotite. Earth Planet Sci Lett 94:364–370.

Frisby, C., Bizimis, M. and Mallick, S. (2016) Seawater-derived rare earth element addition to abyssal peridotites during serpentinization. Lithos 248-251, 432-454.

Fuster, J.M., Fernandez, S., Sagredo, J. (1968). Geologia y Volcanologia de las Islas Canarias. Lanzarote. Inst. Lucas Mallada, Madrid, 177 pp.

Gamal El Dien, H., Arai, S., Doucet, LS. (2019). Cr-spinel records metasomatism not petrogenesis of mantle rocks. Nat Commun 10, 5103.

Geldmacher J., Hoernle K. A., Hanan B. B., Blichert-Toft J., Hauff F., Gill J. B., Schmincke H.-U. (2011). Hafnium Isotopic Variations In East Atlantic Intraplate Volcanism Contrib. Mineral. Petrol. 162, 21-36, Georem-Id: 6115.

Godard M., Lagabrielle Y., Alard O. and Harvey J. (2008). Geochemistry of the highly depleted peridotites drilled at ODP Sites 1272 and 1274 (FifteenTwenty Fracture Zone, Mid-Atlantic Ridge): Implications for mantle dynamics beneath a slow spreading ridge. Earth and Planetary Science Letters, 267, 410–425.

Gómez-Ulla, A., Sigmarsson, O., Huertas, M.J., Devidal, J.L., Ancochea, E. (2018). The historical basanite - alkali basalt - tholeiite suite at Lanzarote, Canary Islands: Carbonated melts of heterogeneous mantle source?, Chemical Geology, Volume 494, 56-68.

Gose, J., Schmädicke, E. & Stalder, R. (2011). Water in mantle orthopyroxene – no visible change in defect water during serpentinization. European Journal of Mineralogy. GeoScienceWorld 23, 529–536.

Govindaraju K. (1995). Working values with confidence limits for twenty-six CRPG, ANRT and IWG-GIT geostandards. Geostandards Newsletter, 19 (Special Issue), 32pp.

Grant K., Ingrin J., Lorand J. P. Dumas P. (2007). Water partitioning between mantle minerals from peridotite xenoliths. Contrib. Mineral. Petrol. 154, 15–34.

Green, D. H., Hibberson, W. O., Kova´ cs, I. & Rosenthal, A. (2010). Water and its influence on the lithosphere–asthenosphere boundary. Nature 467, 448–451.

Guo, X., Bai, J., Wang, C., Wu, X., Zhou, X. (2020). CO2 Induced a Small Water Solubility in Orthopyroxene and Its Implications for Water Storage in the Upper Mantle. American Geophysical Union. Journal of Geophysical Research: Solid Earth Volume 125, Issue 2.

Harvey J., Yoshikawa M., Hammond S. J., Burton K. W. (2012). Deciphering the trace element characteristics in Kil- bourne Hole peridotite xenoliths: melt-rock interaction and metasomatism beneath the Rio Grande Rift, SW USA. J. Petrol. 53, 1709–1742.

Hellebrand, E., Snow, J. E., Dick, H. J. B. & Hofmann, A. W. (2001). Coupled major and trace elements as indicators of the extent of melting in mid-ocean-ridge peridotites. Nature 410, 677–681.

Hirose, K. & Kawamoto, T. (1995). Hydrous partial melting of lherzolite at 1 GPa: The effect of H2O on the genesis of basaltic magmas. Earth and Planetary Science Letters. Elsevier 133, 463–473.

Hirschmann, M. M. (2010). Partial melt in the oceanic low velocity zone. Physics of the Earth and Planetary Interiors. Elsevier B.V. 179, 60–71.

Hirth, G. & Kohlstedt, D. L. (1996). Water in the oceanic upper mantle: implications for rheology, melt extraction and the evolution of the lithosphere. Earth and Planetary Science Letters 144, 93–108.

Hoernle, K. A., Tilton, G., Le Bas, M. J., Duggen, S. & Garbe-Schönberg, D. (2002). Geochemistry of oceanic carbonatites compared with continental carbonatites: mantle recycling of oceanic crustal carbonate. Contributions to Mineralogy and Petrology. Springer-Verlag 142, 520–542.

Humphreys, E.R., Niu, Y., (2009). On the composition of ocean island basalts (OIB): the effects of lithospheric thickness variation and mantle metasomatism. Lithos 112 (1), 118–136.

Ibarrola Munoz E. (1970). Variability Of Basaltic Magmas In The Eastern And Central Canary Islands. Estudios Geol. 26, 337-399.

Jaques, A. L., & Green, D. H., (1980). Anhydrous melting of tholeiitic basalts. Contr. Miner, Petrol. 73, 287-310.

Jochum, K. P. et al. (2011). Determination of Reference Values for NIST SRM 610-617 Glasses Following ISO Guidelines. Geostandards and Geoanalytical Research. John Wiley & Sons, Ltd (10.1111) 35, 397–429.

Johnson, K.T.M., (1998). Experimental determination of partition coefficients for rare earth and high-field-strength elements between clinopyroxene, garnet, and basaltic melt at high pressures. Contrib. Mineral. Petrol. 133, 60–68.

Jones, A.G., Ledo J., Ferguson, I.J., Craven, J.A., Unsworth, M.J., Chouteau, M., Spratt, J.E., (2013a). The electrical resistivity of Canada's lithosphere and correlation with other parameters: contributions from LITHOPROBE and other programs. Can. J. Earth Sci. 51, 573–617.

Justice, M. G., Graham E. K., Tressler R. E., Tsong I.S.T. (1982). The effect of water on high-temperature deformation in olivine. Geophys. Res. Lett. 9, 1005–1008.

Karato, S. (1990). The role of hydrogen in the electrical conductivity of the upper mantle. Nature. Nature Publishing Group 347, 272–273.

Kawamoto, T. (2006). Hydrous phases and water transport in the subducting slab, in Water in Nominally Anhydrous Minerals, ed. by H. Keppler, J.R. Smyth (Mineralogical Society of America, Chantilly, 2006), pp. 273– 289

Khedr, M.Z., Arai, S. (2010). Hydrous peridotites with Ti-rich chromian spinel as a low-temperature forearc mantle facies: evidence from the Happo-O'ne metaperidotites (Japan). Contrib Mineral Petrol 159, 137.

Kinzler, R. J., and T. L. Grove (1992). Primary magmas of mid-ocean ridge basalts: 2. Applications, J. Geophys. Res., 97, 6907–6926.

Klemme S., van der Laan S.R., Foley S.F. and Gunther D (1995) Experimentally determined trace and minor element partitioning between clinopyroxene and carbonatite melt under upper mantle conditions. Earth Planet. Sci. Lett. 133, 439-448.

Kovács, I., Hermann, J., O' Neill, H.S.C., et al., 2008. Quantitative absorbance spectroscopy with unpolarized light: part II. Experimental evaluation and development of a proto- col for quantitative analysis of mineral IR spectra. Am. Mineral. 93, 765–778.

Libowitzky, E. & Bean, A. (2004). IR spectroscopic characterization of hydrous species in minerals. EMU Notes in Mineralogy 6, 227–229.

Lundstrom C. C., Hoernle K. A., Gill J. B. (2003). U-Series Disequilibria In Volcanic Rocks From The Canary Islands: Plume Versus Lithospheric Melting Geochim. Cosmochim. Acta 67, 4153-4177, Georem-Id: 426.

McDonough, W. F. & Sun, S., (1995). The composition of the Earth. Chemical Geology. Elsevier 120, 223–253.

Médard E., Grove T.L., (2008). The effect of H2O on the olivine liquidus of basaltic melts: experiments and thermo- dynamic models. Contrib. Mineral. Petrol. 155, 417–432.

Mosenfelder, J. L. & Rossman, G. R. (2013a). Analysis of hydrogen and fluorine in pyroxenes: I. Orthopyroxene. American Mineralogist.

Mosenfelder, J. L. & Rossman, G. R. (2013b). Analysis of hydrogen and fluorine in pyroxenes: II. Clinopyroxene. American Mineralogist.

Neumann E.-R., Soerensen V. B., Simonsen S. L., Johnsen K. (2000). Gabbroic Xenoliths From La Palma, Tenerife And Lanzarote, Canary Islands: Evidence For Reactions Between Mafic Alkaline Canary Island Melts And Old Oceanic Crust J. Volcanol. Geotherm. Res. 103, 313-342.

Neumann, E., Griffin, W., Pearson, N., and O'reilly, S. Y., (2004). The Evolution of the Upper Mantle beneath the Canary Islands: Information from Trace Elements and Sr isotope Ratios in Minerals in Mantle Xenoliths. Journal of Petrology, 45, 2573-2612.

Neumann, E.R., Wulff-Pedersen, E., (1997). The origin of highly silicic glass in mantle xenoliths from the Canary Islands. Journal of Petrology 38 (11), 1513–1539.

Neumann, E.R., Wulff-Pedersen, E., Johnsen, K., Andersen, T., Krogh, E., (1995). Petrogenesis of spinel harzburgite and dunite suite xenoliths from Lanzarote, eastern Canary Islands: implications for the upper mantle. Lithos 35 (1), 83–107.

Niu, Y. (1997). Mantle Melting and Melt Extraction Processes beneath Ocean Ridges: Evidence from Abyssal Peridotites, Journal of Petrology, Volume 38, Issue 8, Pages 1047–1074.

Novella, D., Frost, D. J., Hauri, E. H., Bureau, H., Raepsaet, C. & Roberge, M. (2014). The distribution of H2O between silicate melt and nominally anhydrous peridotite and the onset of hydrous melting in the deep upper mantle. Earth and Planetary Science Letters. Elsevier 400, 1–13.

Ovchinnikova G. V., Belyatsky B. V., Vasil Eva I. M., Levskii L. K., Grachev A. F., Arana V., Mitjavila I. J. (1995). Sr-Nd-Pb Isotopes Of Mantle Sources Of Basalts From The Canary Islands. Petrologiya 3, 195-206.

Patkó, L., Liptai, N., Előd Aradi, L., Klébesz, R., Sendula, E., Bodnar, R.J., Kovács, I.J., Hidas, K., Cesare, B., Novák, A., Trásy, B., Szabó, C., (2020). Metasomatism-induced wehrlite formation in the upper mantle beneath the Nógrád-Gömör Volcanic Field (Northern Pannonian Basin): Evidence from xenoliths. Geoscience Frontiers. Volume 11, Issue 3, Pages 943-964, ISSN 1674-9871.

Perinelli C, Orlando A, Conte AM, Armienti P, Borrini D, Faccini B, Misiti V (2008) Metasomatism induced by alkaline magma on upper mantle of the Northern Victoria Land (Antarctica): an experimental approach. In: Coltorti M, Gre´goire M (eds) Mantle metasomatism in intra-plate and suprasubduction settings. Geol Soc London Spec Pub 293:197–221.

Peslier, A. H., Francis, D. & Ludden, J. (2002). The Lithospheric Mantle beneath Continental Margins: Melting and Melt-Rock Reaction in Canadian Cordillera Xenoliths. Journal of Petrology. Oxford University Press 43, 2013–2047.

Peslier, A. H. (2010). A review of water contents of nominally anhydrous natural minerals in the mantles of Earth, Mars and the Moon. Journal of Volcanology and Geothermal Research 197, 239–258.

Peslier A.H., Woodland A.B., Bell D.R., Lazarov M., Lapen T.J., (2012). Metasomatic control of water contents in the Kaapvaal cratonic mantle. Geochim. Cosmochim. Acta 97, 213–246.

Peslier, A. H. & Bizimis, M. (2015). Water in Hawaiian peridotite minerals: A case for a dry metasomatized oceanic mantle lithosphere. Geochemistry, Geophysics, Geosystems. John Wiley & Sons, Ltd 16, 1–22.

Peslier, A. H., Bizimis, M. & Matney, M. (2015). Water disequilibrium in olivines from Hawaiian peridotites: Recent metasomatism, H diffusion and magma ascent rates. Geochimica et Cosmochimica Acta 154, 98–117.

Peslier, A. H., Schönbächler, M., Busemann, H. & Karato, S.-I. (2017). Water in the Earth’s Interior: Distribution and Origin. Space Science Reviews 212, 743–810.

Rampone, E., Bottazzi, P. & Ottolini, L. (1991). Complementary Ti and Zr anomalies in orthopyroxene and clinopyroxene from mantle peridotites. Nature. Nature Publishing Group 354, 518–520.

Rivalenti, G., Zanetti, A., Mazzucchelli, M., Vannucci, R. & Cingolani, C. A. (2004). Equivocal carbonatite markers in the mantle xenoliths of the Patagonia backarc: the Gobernador Gregores case (Santa Cruz Province, Argentina). Contributions to MineralogyandPetrology147, 647–670.

Robin-Popieul C.C., Arndt N.T., Chauvel C., Byerly G.R., Sobolev A.V., Wilson A. (2012). A new model for Barberton komatiites: Deep critical melting with high melt retention. Journal of Petrology, 53, 2191–2229.

Roest, W. R., Dannobeitia, J. J., Verhoef, J. & Collette, B. J. (1992). Magnetic anomalies in the Canary Basin and the Mesozoic evolution of the central North Atlantic. Marine Geophysical Research 14, 1–24.

Rospabé, M., Benoit, M., Candaudap, F. (2017). Determination of Trace Element Mass Fractions in Ultramafic Rocks by HR-ICP-MS: A Combined Approach Using a Direct Digestion/Dilution Method and Pre-concentration by Co-precipitation. Geostandards and Geoanalytical Research Vol 42, issue 1, p. 115-129.

Rudnick, R.L., McDonough, F. and Chappell, B.W. (1993) Carbonatite metasomatism in the northern Tanzanian mantle: Petrographic and geochemical characteristics. Earth and Planetary Science Letters 114, 463-475.

Ryan, W.B.F., S.M. Carbotte, J.O. Coplan, S. O'Hara, A. Melkonian, R. Arko, R.A. Weissel, V. Ferrini, A. Goodwillie, F. Nitsche, J. Bonczkowski, and R. Zemsky (2009). Global Multi-Resolution Topography synthesis, Geochem. Geophys. Geosyst., 10, Q03014.

Salters, V. J. M. & Stracke, A. (2004). Composition of the depleted mantle. Geochemistry, Geophysics, Geosystems. Wiley-Blackwell 5, 1–27.

Sambridge, M., Gerald, J.F., Kovács, I., O'Neill, H.S.C., Hermann, J., (2008). Quantitative absorbance spectroscopy with unpolarized light: part I. Physical and mathematical development. Am. Mineral. 93, 751–764.

Schaffer, L., Peslier, A.H., Brandon, A.D., Bizimis, M., Gibler, R., Norman, M., Harvey, J. (2019). Effects of melting, subduction-related metasomatism, and sub-solidus equilibration on the distribution of water contents in the mantle beneath the Rio Grande Rift, Geochimica et Cosmochimica Acta, Volume 266, p. 351-381, ISSN 0016-7037.

Schmincke, H. U., 1982. Volcanic and chemical evolution of the Canary Island. In: Von Rad, V., Hinz, K., Sarnthein, M., & Siebold, S. (eds.) Geology of the North-West African Continental Margin. Berlin: Springer- Verlag, 273-306.

Siena, F., Beccaluva, L., Coltorti, M., Marchesi, S., Morra, V., (1991). Ridge to hot-spot evolution of the Atlantic lithospheric mantle: evidence from Lanzarote peridotite xenoliths (Canary Islands). Journal of Petrology 2, 271–290.

Simons, K., Dixon, J. E., Schilling, J.-G., Kingsley, R. & Poreda, R. (2002). Volatiles in basaltic glasses from the Easter-Salas y Gomez Seamount Chain and Easter Microplate: Implications for geochemical cycling of volatile elements. Geochemistry, Geophysics, Geosystems. Wiley-Blackwell 3, 1–29.

Sun Shen-Su and Hanson G. N. (1975). Origin of Ross Island Basanitoids And Limitations Upon the Heterogeneity of Mantle Sources for Alkali Basalts And Nephelinites Contrib. Mineral. Petrol. 52, 77-106.

Sun Shen-Su. (1980). Lead Isotopic Study of Young Volcanic Rocks from Mid-Ocean Ridges, Ocean Islands and Island Arcs Phil. Trans. Roy. Soc. London A297, 409-445.

Sundvall R., and Stalder R., (2011). Water in upper mantle pyroxene megacrysts and xenocrysts: a survey study. Am. Mineral. 96, 1215–1227.

Thomas L. E., Hawkesworth C. J., Van Calsteren P. W., Turner Simon P., Rogers N. W. (1990). Melt Generation Beneath Ocean Islands: A U-Th-Ra Isotope Study from Lanzarote in the Canary Islands Geochim. Cosmochim. Acta 63, 4081- 4099.

Tielke J.A., Zimmerman M.E., Kohlstedt D.L., (2017). Hydrolytic weakening in olivine single crystals. J. Geophys. Res. 122, 3465–3479.

Vagnes, E. and Amundsen, H.E.F., (1993). Late Cenozoic uplift and volcanism on Spitsbergen: Caused by mantle convection? Geology, 21: 251-254.

Wallace, M.E., Green, D.H., (1988). An experimental determination of primary carbonatite magma composition. Nature 335, 343–346.

Warren, J. M. & Hauri, E. H. (2014). Pyroxenes as tracers of mantle water variations. Journal of Geophysical Research: Solid Earth. John Wiley & Sons, Ltd 119, 1851–1881.

Warren, J. M., (2016). Global variations in abyssal peridotite compositions. Lithos 248-251, 193-219.

Widom E., Hoernle K. A., Shirey S. B., Schmincke H.-U. (1999). Os Isotope Systematics In The Canary Islands and Madeira: Lithospheric Contamination and Mantle Plume Signatures J. Petrol. 40, 279-296.

Wilson, J. T. (1963). A possible origin of the Hawaiian Islands. Canadian Journal of Physics 41, 863–870.

Workman R.K., and Hart S.H., (2005). Major and trace element composition of the depleted MORB mantle (DMM). Earth Planet. Sci. Lett. 231, 53–72.

Yang, X. (2015). OH solubility in olivine in the peridotite-COH system under reducing conditions and implications for water storage and hydrous melting in the reducing upper mantle. Earth and Planetary Science Letters, 432, 199-209.

Yaxley, G. M., Green, D. H. & Kamenetsky, V. (1998). Carbonate metasomatism in the southeastern Australian lithosphere. Journal of Petrology 39, 1917–1930.

Zhang, H., Zheng, J., Zhou, Y., Pan, S., Xiong, Q., Lin, A., & Zhao, Y., (2020). Mesozoic lithospheric modification and replacement beneath the Cathaysia Block: Mineral chemistry and water contents of the Daoxian peridotite xenoliths. Lithos. 358-359, 105385.

Funding sources: NSF grants OCE #1624310 to A.H. Peslier and OCE# 1624315 to M. Bizimis.